



**HAL**  
open science

## Implications for the origin and evolution of Martian Recurring Slope Lineae at Hale crater from CaSSIS observations

G. Munaretto, M. Pajola, Gabriele Cremonese, C. Re, A. Lucchetti, E. Simioni, A. S. McEwen, A. Pommerol, P. Becerra, Susan J. Conway, et al.

► **To cite this version:**

G. Munaretto, M. Pajola, Gabriele Cremonese, C. Re, A. Lucchetti, et al.. Implications for the origin and evolution of Martian Recurring Slope Lineae at Hale crater from CaSSIS observations. *Planetary and Space Science*, 2020, 187, pp.104947. 10.1016/j.pss.2020.104947 . hal-02614604

**HAL Id: hal-02614604**

**<https://hal.science/hal-02614604>**

Submitted on 8 Dec 2023

**HAL** is a multi-disciplinary open access archive for the deposit and dissemination of scientific research documents, whether they are published or not. The documents may come from teaching and research institutions in France or abroad, or from public or private research centers.

L'archive ouverte pluridisciplinaire **HAL**, est destinée au dépôt et à la diffusion de documents scientifiques de niveau recherche, publiés ou non, émanant des établissements d'enseignement et de recherche français ou étrangers, des laboratoires publics ou privés.

# Implications for the origin and evolution of Martian recurring slope lineae at Hale crater from CaSSIS observations

G. Munaretto<sup>a,b,\*</sup>, M. Pajola<sup>a</sup>, G. Cremonese<sup>a</sup>, C. Re<sup>a</sup>, A. Lucchetti<sup>a</sup>, E. Simioni<sup>a</sup>, A. S. McEwen<sup>c</sup>, A. Pommerol<sup>d</sup>, P. Becerra<sup>d</sup>, S. J. Conway<sup>e</sup>, N. Thomas<sup>d</sup>, M. Massironi<sup>a,f</sup>

<sup>a</sup>*INAF, Osservatorio Astronomico di Padova, Padova, Italy*

<sup>b</sup>*Department of Physics and Astronomy “G. Galilei”, University of Padova, Padova, Italy*

<sup>c</sup>*Lunar and Planetary Laboratory, University of Arizona, Tucson, Arizona, USA*

<sup>d</sup>*Physikalisches Institut Universität Bern, Switzerland*

<sup>e</sup>*CNRS Laboratoire de Planétologie et Géodynamique de Nantes, Université de Nantes, 2 rue de la Houssinière, 44322 Nantes, France*

<sup>f</sup>*Department of Geosciences, University of Padova, Padova, Italy*

---

## Abstract

Recurring Slope Lineae (RSL) are narrow, dark features that typically source from rocky outcrops, incrementally lengthen down Martian steep slopes in warm seasons, fade in cold seasons and recur annually. In this study we report the first observations of RSL at Hale crater, Mars, during late southern summer by the Colour and Surface Science Imaging System (CaSSIS) on board ESA’s ExoMars Trace Gas Orbiter (TGO). For the first time, we analyze images of RSL acquired during morning solar local times and compare them with High Resolution Imaging Science Experiment (HiRISE) observations taken in the afternoon. We find that RSL activity is correlated with the presence of steep slopes. Our thermal analysis establishes that local temperatures are high enough to allow either the melting of brines or deliquescence

---

\*Corresponding author

*Email address:* `giovanni.munaretto.1@phd.unipd.it`, `munarettogiovanni@gmail.com`  
(G. Munaretto)

of salts during the observation period, but the slope and aspect distributions of RSL activity predicted by these processes are not consistent with our observations. We do not find any significant relative albedo difference between morning and afternoon RSL. Differences above 11% would have been detected by our methodology, if present. This instead suggests that RSL at Hale crater are not caused by seeping water that reaches the surface, but are best explained as dry flows of granular material.

*Keywords:* Recurring slope Lineae, RSL, CaSSIS, HiRISE, Mars, Relative albedo, THEMIS

---

## 1. Introduction

The origin of Recurring Slope Lineae (RSL) is one of the most controversial science questions regarding present-day surface activity on Mars. They appear as narrow ( $< 5$  m) low-albedo streaks, often starting from bedrock outcrops and lengthening hundreds of meters down Martian steep slopes at equatorial and mid-latitudes (McEwen et al., 2011). RSL generally start lengthening during warm seasons, fade during cold ones and recur over multiple Martian years. However, RSL activity can be more complicated than a simple repeating cycle of lengthening and fading, as several well studied sites shows simultaneous lengthening, appearance and fading of RSL (Stillman and Grimm, 2018; Vincendon et al., 2019). Many models have been proposed to explain their origin, but a definitive explanation is still elusive. These can be broadly summarized in three classes: *wet models*, in which RSL are water-dominated features, *dry models*, that explain RSL as dry mass fluxes or aeolian features, and *hybrid models*, in which water plays an indirect role in RSL formation and lengthening.

16 *1.1. Wet models*

17 The temperature dependence of RSL activity suggests that water or brines may  
18 be present (McEwen et al., 2011; McEwen et al., 2014; Stillman et al., 2014; Hu-  
19 ber et al., 2020). Spatial correlation with multi-scale fractures appears to support  
20 groundwater sources (Stillman et al., 2016; Abotalib and Heggy, 2019). However,  
21 topographic relationships cast doubts on these models, as they explain the season-  
22 ality of RSL activity, but require larger volumes of liquids than could be reasonably  
23 present on Mars at these latitudes (Grimm et al., 2014; Chojnacki et al., 2016).  
24 Moreover, many RSL source from local topographic highs, such as ridge crests or  
25 peaks, where a groundwater source is unlikely (Chojnacki et al., 2016). Another wet  
26 process that has been considered to explain RSL formation is the deliquescence of  
27 salts, which occurs when hygroscopic salts absorb water vapor to form a liquid solu-  
28 tion (Gough et al., 2016). For this to happen, temperatures higher than the eutectic  
29 temperature of the solution and relative humidities (RH) greater than their deliques-  
30 cence relative humidity (DRH) are required (Gough et al., 2016). Several laboratory  
31 studies have identified chlorides (Gough et al., 2016; Wang et al., 2019), perchlorates  
32 (Nuding et al., 2014) and chlorates (Toner and Catling, 2018) as potential candidate  
33 deliquescent salts. The required RH values for the deliquescence of  $\text{CaCl}_2$  brines  
34 range from 12.9% when  $T = 273$  K to  $\sim 20.9\%$  at  $T = 233$  K (Gough et al., 2016),  
35 while their eutectic temperature is  $T = 223\text{K}$ . Numerical modeling by Gough et al.  
36 (2016) showed that atmospheric water vapor could sustain the deliquescence of hy-  
37 drated  $\text{CaCl}_2$  brines at 3-cm depth at the Phoenix landing site. However, it is not  
38 clear whether or not the same process can happen at RSL sites (Gough et al., 2016),

39 even though Wang et al. (2019) recently proposed that the deliquescence of sub-  
40 surface hydrated chlorides can be a thermodynamically viable (but not necessarily  
41 sufficient) process for triggering RSL activity. The deliquescence of Ca-perchlorates  
42 is also interesting because of their relatively low DRH (from  $10 \pm 4\%$  at 273 K to  
43  $55 \pm 4\%$  at 223 K (Nuding et al., 2014)) and eutectic temperature of  $T = 200$  K.  
44 Finally, chlorates may be even more interesting candidates as they have a lower DRH  
45 than perchlorates (Toner and Catling, 2018).

## 46 1.2. Dry models

47 In these models, RSL lengthening and formation are interpreted with dry mech-  
48 anisms involving granular flows or aeolian processes (Dundas et al., 2017; Schmidt  
49 et al., 2017; Vincendon et al., 2019; Schaefer et al., 2019). These have been initially  
50 invoked to explain the correlation between the angle of repose of granular material  
51 and the slope angle at which RSL stop (Dundas et al., 2017), although more re-  
52 cent measurements show that  $\sim 25\%$  of RSL reach slopes below the angle of repose  
53 (Tebolt et al., 2020; Stillman et al., 2020). In addition, Schmidt et al. (2017) dis-  
54 cussed morphological inconsistencies between RSL and wet flows, such as the lack of  
55 terminal or lateral levees; Vincendon et al. (2019) proved that RSL formation occurs  
56 outside the time-frame compatible with the existence of liquid water and does not  
57 show a preference for the warmest slopes. Finally, the spectral detection of hydrated  
58 salts at some RSL sites (Ojha et al., 2015), which would support the presence of  
59 liquids, was recently proven to not be robust (Leask et al., 2018; Vincendon et al.,  
60 2019). Although dry flows do not require a source of water, a trigger mechanism has  
61 not been fully established yet. Schmidt et al. (2017) proposed a Knudsen pump as a

62 trigger mechanism, but it doesn't predict RSL at the times and locations where they  
63 are observed (Stillman and Grimm, 2018; Vincendon et al., 2019). Vincendon et al.  
64 (2019) and Schaefer et al. (2019) proposed that RSL are aeolian features resulting  
65 from the removal of bright dust by winds. A fading mechanism has been recently  
66 proposed by Vincendon et al. (2019), which showed that the progressive brightening  
67 of RSL can be attributed to dust deposition. On the other hand Schaefer et al. (2019)  
68 discovered that the fading of RSL is similar to that of other dust-related albedo fea-  
69 tures (dust devil tracks, rockfalls) on the basis of relative albedo analyses at Tivat  
70 crater ( $45^\circ$  S,  $9^\circ$  E). They propose that RSL fade due to the widespread removal  
71 of dust from the neighboring slopes, which progressively darken until matching the  
72 RSL reflectance. While this mechanism applies well to Tivat crater, it cannot explain  
73 the concurrent fading and lengthening of RSL observed in several other RSL sites  
74 (Vincendon et al., 2019; Stillman et al., 2020).

### 75 *1.3. Hybrid models*

76 Other hypotheses envision an indirect role of water in triggering RSL activity.  
77 Massé et al. (2016) showed that boiling fresh water can trigger granular flows by vio-  
78 lently displacing grains. While this model is interesting because it requires less water  
79 than wet-based models, boiling water requires high temperatures that are hardly met  
80 at the onset of RSL activity in early spring (Stillman and Grimm, 2018; Vincendon  
81 et al., 2019). More recently, Shoji et al. (2019) proposed that moisture serves to  
82 stabilize steep slopes in cold seasons, which flow when drying during the warm sea-  
83 sons. In addition, Bishop et al. (2019) proposed that subsurface brine activity can  
84 create surface collapse features, perhaps initiating RSL when on steep enough slopes.

85

86 The High Resolution Imaging Science Experiment (HiRISE, McEwen et al. (2007))  
87 on board the NASA's Mars Reconnaissance Orbiter (MRO) mission is the optimal  
88 instrument to image RSL due to its high pixel scale ( $\sim 0.3$  m/pixel), which allows  
89 for digital terrain models (DTM) at  $\sim 1$  m spatial resolution. However, the Sun-  
90 synchronous orbit of MRO limits observation times between  $\sim 2$ -4 PM, during the  
91 local afternoon.

92 The Colour and Surface Imaging System (CaSSIS, Thomas et al. (2017)), on board  
93 the ESA ExoMars Trace Gas Orbiter (TGO) mission, images the Martian surface  
94 at 4.6 m/pixel in four color bands. It carries a rotation mechanism that allows it  
95 to acquire stereo observations with identical illumination angles for the production  
96 of DTMs. The  $74^\circ$  inclined orbit of TGO allows CaSSIS to observe the surface  
97 at different times of day, such as the local morning. This capability is pivotal for  
98 RSL studies, since morning observations of these features are not possible other-  
99 wise. The only exceptions are extremely early morning views by Mars Odyssey, with  
100 poor SNR and much lower spatial resolution. Morning activity can provide great  
101 insights on the nature and formation mechanism of RSL. Laboratory studies (Gough  
102 et al., 2016) and analyses of data from both the Rover Environmental Monitoring  
103 Station (REMS) on board Curiosity and the Thermal and Electrical Conductivity  
104 Probe (TECP) on the Phoenix lander shows that daily maximum RH values occur  
105 during the early morning of local summer (Steele et al., 2017; Fischer et al., 2019),  
106 suggesting that these local hours are the most favourable for deliquescence. If RSL  
107 are liquid-based flows, their activity should increase in the morning, when both tem-

108 perature and air humidity are high enough to favor the deliquescence of salts and  
109 increase the stability of brines. Under this scenario, dehydration would occur in the  
110 afternoon, so we would also expect RSL to be darker in the morning than in the  
111 afternoon. Instead, if RSL are caused by the melting of shallow subsurface ice (such  
112 as from a deep groundwater source), then they should be darker in the afternoon.  
113 This assumes that the quantity of water or brines at play is relatively small, so that  
114 evaporative losses exceed the supply of water (Hillel, 2004). If instead RSL have a  
115 high water content, pore water concentration would not be affected by evaporation  
116 and there wouldn't be any albedo change (Pommerol et al., 2013; Levy et al., 2014).  
117 The latter case, however, may not be in agreement with the very low water content  
118 of RSL estimated at Garni crater (Edwards and Piqueux, 2016). Finally, if RSL are  
119 dry flows, then we do not expect any albedo change between the observations.

120 In this study we present the first observations of RSL performed by CaSSIS during  
121 the local morning and compare them with HiRISE observations acquired one month  
122 earlier in the afternoon. In particular, we search for any differences in their over-  
123 all morphology (i.e. length, slope, aspect) and report relative albedo measurements  
124 performed on morning and afternoon images. We analyze the thermal conditions of  
125 the surface and shallow sub-surface at the time of the CaSSIS observation to assess  
126 whether temperatures would either allow melting of brines or deliquescence of salts.

## 127 **2. Data**

128 The study region is the central peak of Hale crater ( $-35.7^\circ$  N,  $323.5^\circ$  E, see figures  
129 (2a, b)), where several areally extensive RSL have been discovered so far, making it



130 an ideal site to be investigated with CaSSIS. RSL in Hale were first reported by Ojha  
131 et al. (2014) and then analyzed by different authors (Stillman et al., 2014; Dundas  
132 et al., 2017; Stillman and Grimm, 2018). Stillman and Grimm (2018) reported that  
133 RSL activity in general may occur in one or two pulses, where RSL fade partially or  
134 completely and then re-appear in the same year. The RSL at Hale crater are peculiar  
135 because they seem to experience three pulses of activity (Stillman and Grimm, 2018),  
136 unlike any other sites analyzed on Mars so far. Our RSL observations span an  $L_s$   
137 range between  $331.5^\circ$  and  $347.4^\circ$ , within the third pulse proposed by Stillman and  
138 Grimm (2018), allowing us to confirm its presence at Hale crater. In order to study  
139 whether there is a diurnal dependence in the activity of RSL, an ideal dataset would  
140 include two observations of an RSL site acquired during the same Martian day,  
141 the first one with CaSSIS in the morning and the second one with HiRISE in the  
142 afternoon. In our case, the observations were acquired during late southern summer,  
143 one month apart. The HiRISE image was acquired on  $L_s = 331.5^\circ$  at 14:06 local time,  
144 while the CaSSIS image was acquired on  $L_s = 347.4^\circ$  at 11:13 local time. This time  
145 interval may be too big to minimize seasonal changes between images, such as fading  
146 of RSL, which typically happens during this season at southern hemisphere sites.  
147 However, this issue may not be important for Hale crater, where fading was reported  
148 to occur only after  $L_s > 7^\circ$  for both MY 30 and 31 (Stillman and Grimm, 2018),  
149 well after the  $L_s$  of our observations. For this reason, we are confident that fading is  
150 not influencing our analysis. Moreover, RSL at Hale crater are “rejuvenated” by a  
151 third pulse of activity which occurs just before  $L_s = 331.5^\circ$ . The occurrence of this  
152 third pulse of activity is illustrated in figure (1). HiRISE image ESP\_057\_569\_1440,

153 acquired at  $L_s = 286.6^\circ$ , shows dense RSL coverage (see fig. 1a), while the subsequent  
154 HiRISE image ESP\_058618\_1445, acquired at  $L_s = 331.5^\circ$ , shows smaller RSL in the  
155 same places (see fig. 1b). These further lengthened in the subsequent CaSSIS image  
156 MY34\_005640\_218\_2, acquired at  $L_s = 347.4^\circ$  (see fig. 1c). This means that the RSL  
157 had completely faded and had started lengthening again between the first two images  
158 (1a,b) and continued lengthening between  $L_s = 331.5^\circ$  and  $L_s = 347.4^\circ$ . This is also  
159 confirmed by the analysis of HiRISE images of Hale crater in previous Martian Years  
160 reported by Stillman and Grimm (2018). In particular, from figure S9 of Stillman  
161 and Grimm (2018) we see that RSL lengthening occurs between  $341.9^\circ < L_s < 7^\circ$   
162 in MY 31 and  $326.5^\circ < L_s < 7^\circ$  MY 32. This means that despite the HiRISE and  
163 CaSSIS images analyzed here being taken 30 days apart, the mechanisms responsible  
164 for RSL lengthening are active during this period and any seasonal fading can be  
165 considered negligible, allowing us to compare RSL albedos between the two images.  
166 In the following sections we will describe our dataset, summarized in figure (2), which  
167 combines HiRISE (section 2.1), CaSSIS (section 2.2) and Thermal Emission Imaging  
168 System (THEMIS; Christensen et al. (2004)) (section 2.3) observations. Image IDs  
169 and observation details for each of the products we used are detailed in Appendix  
170 A.

### 171 *2.1. HiRISE data*

172 We used the latest publicly available HiRISE image of the central peak of Hale  
173 crater, ESP\_058618\_1445, acquired on 27 January 2019 at 14:06 Mars local time  
174 and with a  $L_s = 331.5^\circ$ , as well as the corresponding HiRISE DTM and orthophoto  
175 of the region. The RED channel (McEwen et al., 2007) of the HiRISE image was

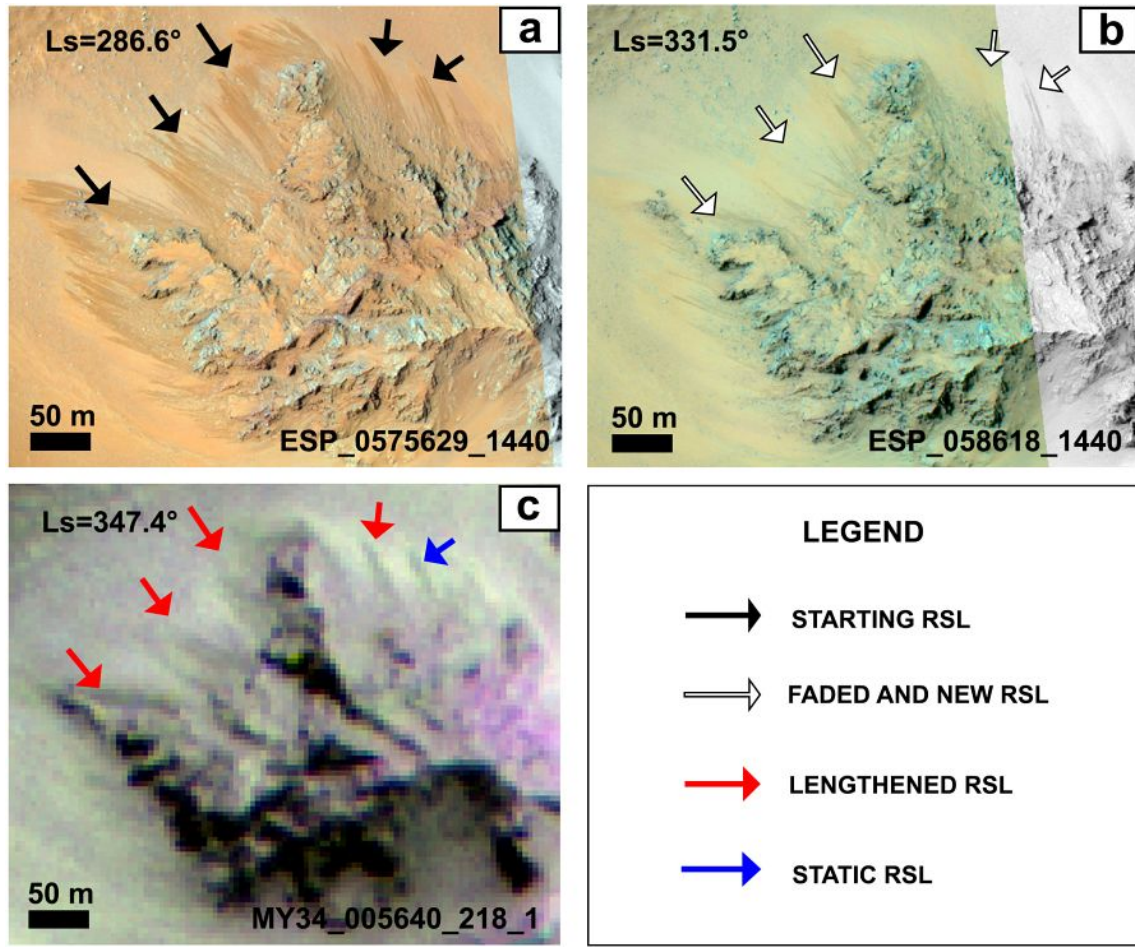


Figure 1: RSL activity during the 3rd pulse at Hale crater. a) HiRISE image showing areally extensive RSL, indicated by black arrows, at  $L_s = 286.6^\circ$ . b) The same area but observed at  $L_s = 331.5^\circ$ . White arrows indicate the same RSL in a) that faded and restarted their lengthening phase. c) Colour composite of the RED, PAN and BLU filters of CaSSIS image MY34\_005640\_218\_2 taken at  $L_s = 347.4^\circ$  and showing that some a RSL in n) remained static (blue arrow) while others (red arrows) further lengthened with respect to the previous image. Areal extents of RSL in this area are mapped in figure (10).

176 orthorectified on the DTM using the NASA Ames Stereo Pipeline (Moratto et al.,  
177 2010). To obtain reliable slope and aspect measurements, we adapted the technique  
178 of Schaefer et al. (2019) to reduce noise and systematic artifacts present in the DTM  
179 and calculated slope and aspect maps using ArcGIS (Burrough and McDonell, 1998).  
180 In particular, the DTM was resampled at 2m resolution and smoothed with a 10 m  
181 radius moving average as in (Schaefer et al., 2019). The aligned HiRISE DTM, image,  
182 aspect and slope maps are shown in figure (2). More details about the HiRISE data  
183 products used in the analysis are provided in Appendix A.

## 184 *2.2. CaSSIS data*

185 The central peak of Hale crater was imaged by CaSSIS on 26 February 2019 at  
186 11:13 Mars local time, with a  $L_s = 347.4^\circ$ , in stereo mode and with the near infrared  
187 (NIR), red (RED), panchromatic (PAN) and blue (BLU) filters (Thomas et al.,  
188 2017). From the CaSISS stereo pair MY34.005640\_218\_1, a DTM and radiometrically  
189 calibrated orthophoto of the PAN channel of the second image in the stereo pair  
190 (i.e. MY34.005640\_218\_2) were obtained using the 3DPD photogrammetric pipeline  
191 described in Simioni et al. (2017). The CaSSIS orthophoto was then manually co-  
192 registered to the aligned HiRISE dataset in ArcGIS. The footprint of the CaSSIS  
193 stereo pair is shown in figure (2b) and a color composite image obtained by combining  
194 the overlap of the RED, PAN and BLU channels is shown in figure (2c).

## 195 *2.3. THEMIS data*

196 We used the MARSTHERM web interface (Putzig et al., 2013) to process THEMIS  
197 infrared observations within  $\pm 5^\circ$  of  $L_s$  of the CaSSIS image and derive thermal in-

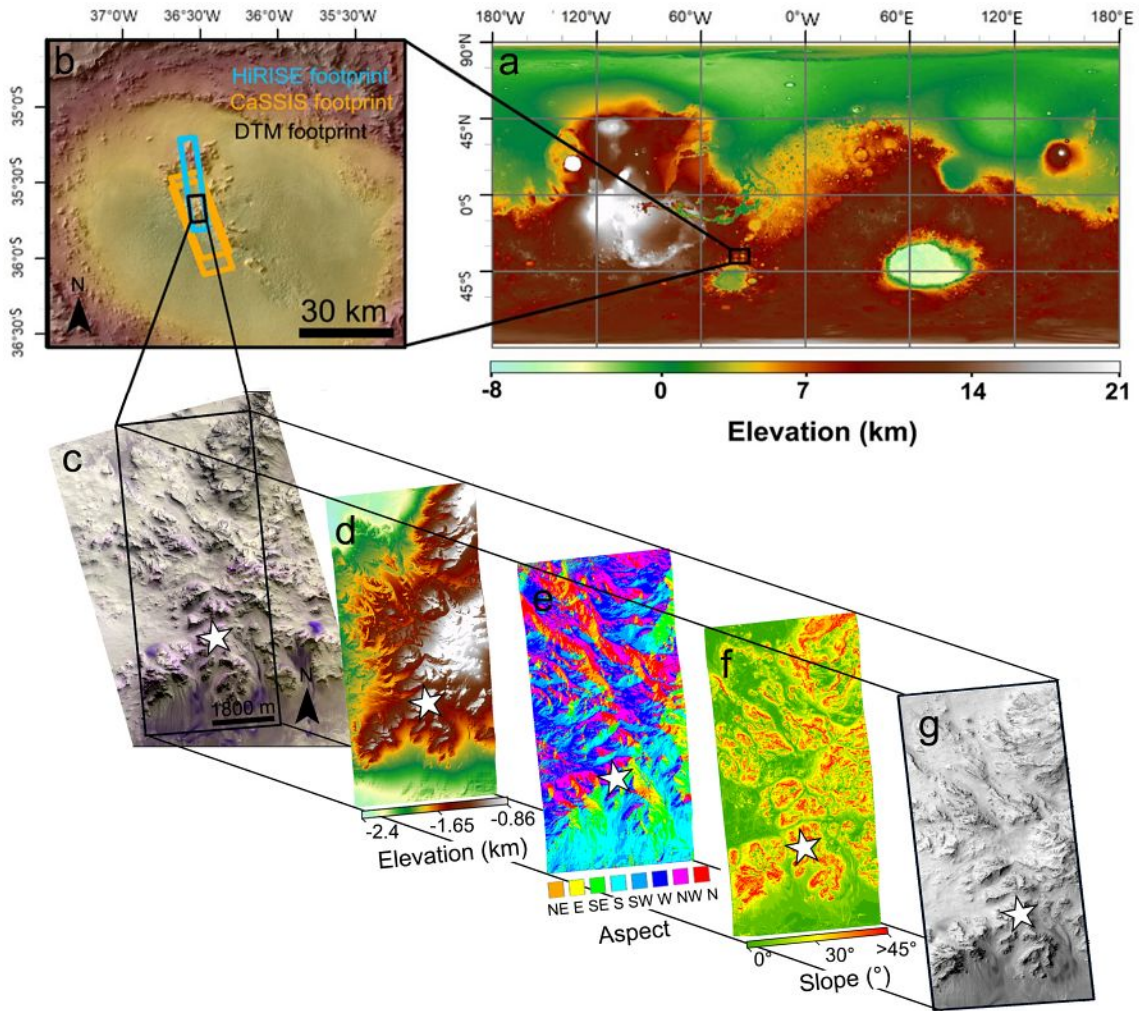


Figure 2: Schematic description of our dataset. a) Mars Orbiter Laser Altimeter (MOLA) colorized elevation map of Mars showing the location of Hale crater (black rectangle). b) MOLA colorized elevation map overlaid on THEMIS infrared daytime mosaic showing the central peak of Hale crater and the footprints of our observations. c) RGB color composite of the RED, PAN and BLU filters of CaSSIS image MY34\_005640\_218\_2 depicting the central peak of Hale crater. d) HiRISE DTM, e) aspect and f) slope maps generated from the HiRISE DTM and g) HiRISE image ESP\_058618\_1445 projected onto the HiRISE DTM. The white star indicates the location of figure (1).

198 ertia maps of Hale crater at 100 m resolution. As is customary for Martian thermal  
199 modeling studies (Edwards and Piqueux, 2016; Fergason et al., 2006), we considered  
200 only nighttime observations. The final thermal inertia map was obtained by comput-  
201 ing the median thermal inertia value at each pixel from all the selected observations.  
202 The thermal inertia map was then used to simulate surface and subsurface temper-  
203 atures at Hale crater, as described in section (3.3).

### 204 **3. Methods**

#### 205 *3.1. General properties*

206 We first identified all RSL that were resolved in both the HiRISE and CaSSIS  
207 images. Sometimes the RSL identified on the HiRISE image occurred in clusters  
208 of several lineae, spanning multiple CaSSIS pixels, but separated by distances lower  
209 than the CaSSIS resolution. In these cases we did not consider the single RSL, not  
210 resolved by CaSSIS, but the whole cluster. We mapped the envelope of each RSL,  
211 or cluster of RSL, in both images. To better compare the two images and cross-  
212 check any detected lengthening, we also resampled the HiRISE image at the CaSSIS  
213 resolution by summing all HiRISE pixels within a CaSSIS pixel and mapped the  
214 RSL envelopes on the resampled image. Examples of “changed” and “static” RSL,  
215 including their mapped envelopes are seen in figure (3). If a significant RSL length-  
216 ening could be detected using both the original and resampled images, we labeled  
217 the RSL as “changed”, otherwise as “static”. To take into account uncertainties in  
218 the comparison from any residual misalignment and/or differences in resolution and  
219 illumination between the two images, we considered a lengthening to be statistically

220 robust only if greater than 1 CaSSIS pixel. This threshold is much lower than the  
221 typical lengthening that should occur between the two images,  $\sim 60-100$  m given the  
222 average RSL advance rates (Levy, 2012; Stillman et al., 2016). To distinguish dark-  
223 ening caused by illumination conditions (i.e. topographic shading) from real RSL in  
224 the CaSSIS image we also considered the relative orientation between the slopes and  
225 the direction of the Sun, and avoided comparison of albedo features within highly  
226 shaded regions. Finally, we measured the mean slope and aspect at the termination  
point of every mapped RSL in the HiRISE image.

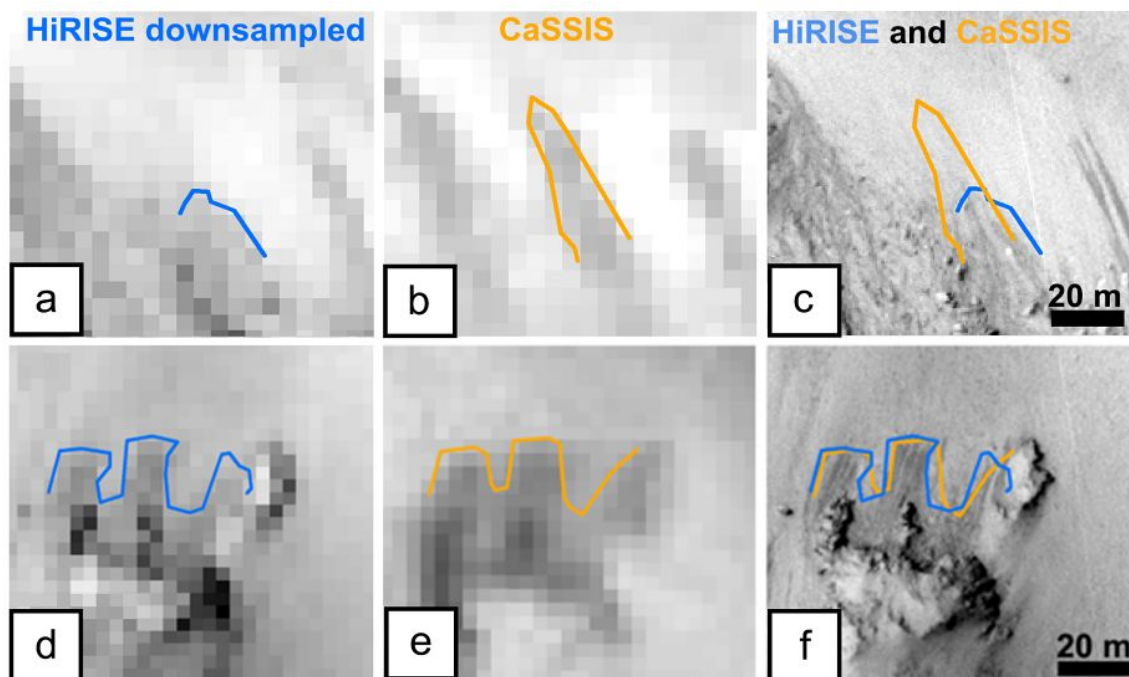


Figure 3: Examples of “changed” (upper row) and “static” (lower row) RSL envelopes mapped in blue on the downsampled afternoon HiRISE image (a,d) and in orange on the morning CaSSIS image (b,e). Panels (c) and (f) Show their comparison on top of the original HiRISE image.

227



228 *3.2. Relative albedo*

229 The relative albedo is the ratio between the reflectance (I/F) of two atmospher-  
230 ically corrected regions of the surface that have the same illumination conditions  
231 (Daubar et al., 2016). Our goal is to assess if RSL are darker, and thus potentially  
232 wetter, in the morning with respect to the afternoon. We compute the RSL relative  
233 albedo as the ratio between the reflectance of an RSL region and the reflectance of  
234 a nearby RSL-free region with the same illumination conditions, that is assumed to  
235 not have “changed”. We only compare the CaSSIS PAN channel with the HiRISE  
236 RED channel. As these two filters closely correspond one to each other, the consis-  
237 tency between HiRISE and CaSSIS measurements is granted (Thomas et al., 2017).  
238 A complete multi-band analysis taking into account for differences between the CaS-  
239 SIS RED and NIR and the HiRISE IR filters is left for a future work. In order to  
240 perform relative albedo measurements, it is necessary to first identify regions with  
241 similar slope and aspect, and in turn similar incidence angles. To do this, we first  
242 selected a set of regions of interest (ROI) from the previously identified RSL in both  
243 images (RSL ROI). To ensure that each RSL ROI is dominated by RSL signal, we  
244 used the HiRISE image for the selection and kept that same ROI in the CaSSIS  
245 image. Their mean slope and aspect were measured using ArcGIS. For each RSL  
246 ROI, we defined a corresponding background (BK) ROI in a nearby region, with  
247 similar mean slope and aspect but without RSL in either images. Where a suitable  
248 BK ROI could not be found, we did not include the RSL in the relative albedo anal-  
249 ysis. This criterion proved to be the most restrictive, resulting in a relatively low  
250 number of suitable ROIs for relative albedo measurement, as discussed in section



251 (4.2). Figure (4) shows examples of some selected ROIs. We extracted the mean  
 252 I/F and its standard deviation for each BK and RSL ROI and applied a first order  
 253 atmospheric correction by subtracting the I/F value of the darkest pixel within shad-  
 254 ows in the overlapping region of the two images from  $IF_{RSL}$ . To take into account  
 255 the different resolutions of the two images, for HiRISE we used the mean I/F in a  
 256  $4.6 \times 4.6$  m square area around the darkest pixel within shadows. Although this kind  
 257 of atmospheric correction can be inaccurate in steep topography, it is often adopted  
 258 when performing relative photometry (Daubar et al., 2016; Schaefer et al., 2019). In  
 259 addition, more precise use of shadows areas for this purpose could be performed if  
 260 required (Hoekzema et al., 2011). In our case, however, we only apply the atmo-  
 261 spheric correction to the RSL ROIs and not to the BK ones. The rationale behind  
 262 this approach is to take into account the non-linear effect of aerosols on the apparent  
 263 reflectance of a surface, meaning that low-albedo surfaces are more brightened by  
 264 diffuse light than high albedo ones (Vincendon et al., 2007). We finally computed  
 265 the relative albedo as:

$$RA_* = \frac{IF_{RSL} - IF_D}{IF_{BK}} \quad * \in \{H, C\} \quad (1)$$

266 where  $RA_*$  is the RSL relative albedo, computed either from the original HiRISE  
 267 ( $* = H$ ) or CaSSIS ( $* = C$ ) images.  $IF_{RSL}$  is the mean I/F extracted from an  
 268 RSL ROI.  $IF_D$  is the I/F of the darkest shadowed pixel and  $IF_{BK}$  is the I/F of  
 269 a BK ROI. We compute uncertainties for the HiRISE and CaSSIS relative albe-  
 270 dos applying standard error propagation (see Appendix B). The significance of any  
 271 difference between the HiRISE and CaSSIS relative albedos is established applying

272 standard statistical tests. We use the Kolmogorov-Smirnov (*KS*, Massey (1951))  
273 and Wilcoxon (*W*, Wilcoxon (1945)) signed-rank statistical tests to assess if the  
274 HiRISE and CaSSIS relative albedos are sampled from the same distribution. We  
275 apply the Anderson-Darling (*AD*, Anderson and Darling (1954)) and Shapiro-Wilk  
276 statistical tests (*SW*, Shapiro and Wilk (1965)) to assess if the differences between  
277 the two distributions are stochastic. From each test, a  $p$ -value is computed and  
278 compared with the customary 0.05 threshold. All tests and the  $p$ -value compu-  
279 tations are performed using routines implemented in the `nortest` library (Gross  
280 and Ligges, 2015) (<https://CRAN.R-project.org/package=nortest>) of the R pro-  
281 gramming language (R Core Team, 2019).

### 282 *3.3. Thermal analysis*

283 We simulated diurnal surface and subsurface temperatures on the region depicted  
284 in figure (5a) at the time of the CaSSIS observation using the thermal model of  
285 Schorghofer et al. (2019). This model solves the 1D thermal balance and diffusion  
286 equations in a rough surface, taking into account the contribution of 3D topography  
287 to the surface energy balance. Examples of modeled diurnal surface and subsurface  
288 temperature maps are shown in figure (6). We focused only on this region because  
289 it hosts many large RSL on multiple slope orientations and allowed us to reduce  
290 computation time. Within this region we defined different study zones, as depicted  
291 in figure (5b). To account for the different thermal behavior of different materials  
292 within our region, we distinguished between zones composed of exposed bedrock (i.e.  
293 those starting with “B” in figure (5d) and zones composed of finer material, like  
294 regolith (i.e. those starting with “S” in figure (5d)). For the former we estimate a

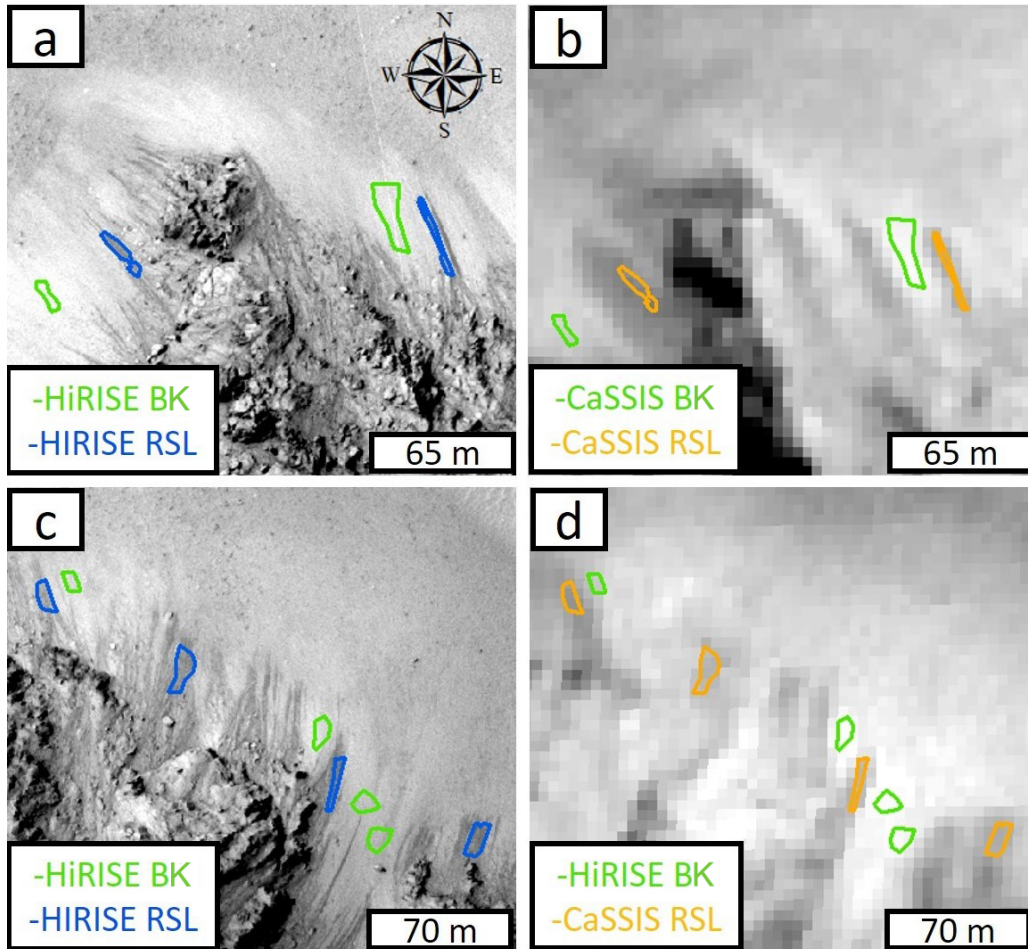


Figure 4: a,c): examples of RSL ROI (blue) and BK ROI (green) used to extract the mean I/F of RSL and RSL-free regions and their uncertainty from the HiRISE image. b,d): examples of RSL (orange) and BK (green) ROIs used to extract the mean I/F of RSL and RSL-free regions and their uncertainty from the CaSSIS orthoimage.

295 mean thermal inertia of  $772^{+188}_{-130}$  TIU, and for the latter we estimate a mean thermal  
 296 inertia of  $540^{+128}_{-122}$  TIU (TIU is thermal inertia units, i.e.  $\text{J m}^{-2} \text{s}^{-0.5} \text{K}^{-1}$ ). Thermal  
 297 inertia and  $3\sigma$  uncertainties were estimated by computing the mean, maximum and  
 298 minimum values of pixels within the “BEDROCK” and “SLOPE” ROIs defined in

299 the thermal inertia map and depicted in figure (5d). These estimates are used, along  
300 with a DTM of the region, to simulate the mean, maximum and minimum diurnal  
301 temperature profiles at the surface and at 10 and 20 cm depth, as in (Chevrier and  
302 Rivera-Valentin, 2012). Although the thermal model has already been validated by  
303 Schorghofer et al. (2019) at Palikir crater, we also checked that the simulated tem-  
304 peratures of our zones agreed with the nighttime THEMIS IR observation I59655010,  
305 acquired at a  $L_s = 348.8^\circ$ , close to the CaSSIS image  $L_s$ . THEMIS surface temper-  
306 atures were obtained using the <https://www.thmproc.mars.asu.edu> website and  
307 are reported in figure (9).

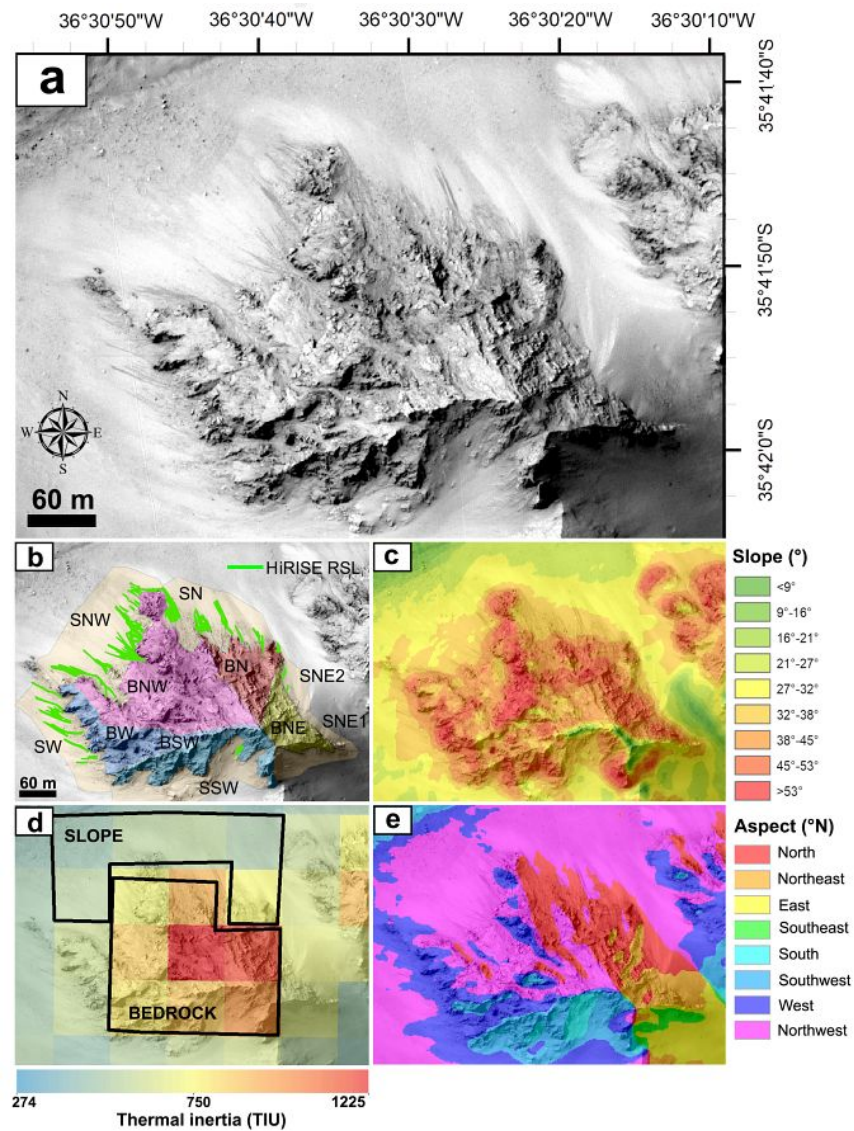


Figure 5: a) HiRISE image ESP\_058618\_1445 showing the selected region for the thermal analysis. b) Definition of zones where we simulated temperature profiles. c) Slope map. d) THEMIS-derived thermal inertia map. Black polygons represent the “BEDROCK” and “SLOPE” ROIs used to extract the thermal inertia of the bedrock material and the regolith, respectively. e) Aspect map.

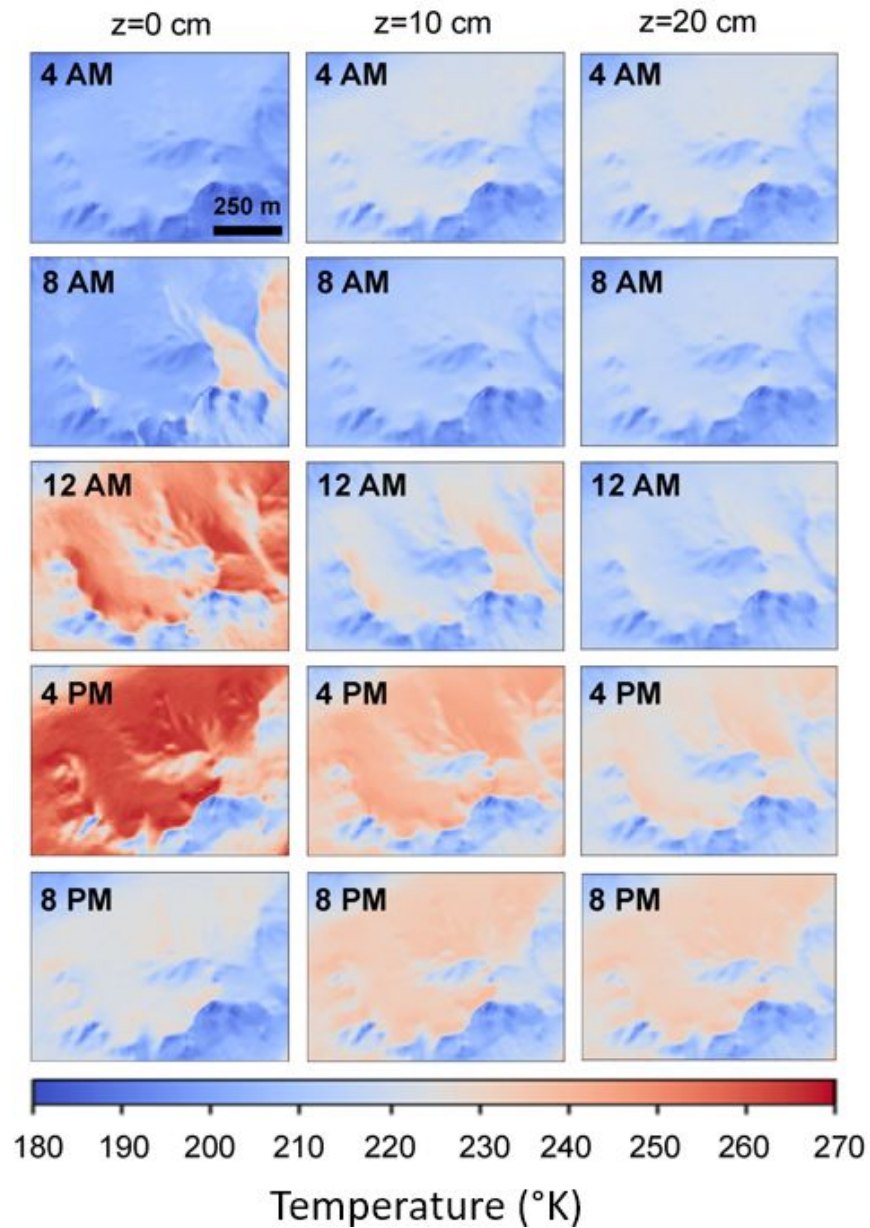


Figure 6: Example of diurnal temperature maps simulated at the surface (left), 10 cm depth (middle) and 20 cm depth (right). The simulations were performed using a THEMIS-derived thermal inertia of 770 TIU and used to extract diurnal temperature profiles for the bedrock.

## 308 4. Results

### 309 4.1. General properties

310 We identified 125 RSL, or groups of RSL in some cases, that were visible in  
311 both the HiRISE and CaSSIS images. Figures (7b,c and d) show examples of RSL  
312 as observed by CaSSIS. All the mapped RSL and their classification in terms of  
313 significant or absent lengthening between the morning and afternoon image are shown  
314 in figure (7a), while their slope and aspect distribution are in figures (8a,b) . In  
315 particular, the aspect distribution in figure (8b) shows that the considered RSL are  
316 found on north, north-west and west facing slopes and that there is no significant  
317 difference between the aspect of “static” and “changed” RSL. On the contrary, the  
318 slope distribution shows a dichotomy between the two classes. Most of the “static”  
319 RSL are found at slopes  $< 30^\circ - 32^\circ$  while most of “changed” RSL are found at  
320 slopes  $> 30^\circ - 32^\circ$ .

### 321 4.2. Relative albedo analysis

322 We performed the relative albedo analysis on a selected sample of 11 RSL. The  
323 relatively low number of RSL considered for the relative albedo analysis is determined  
324 by the selection criteria discussed in section (3.2), i.e. we selected only RSL ROIs  
325 for which we could identify nearby BK ROIs having their same slope and aspect. In  
326 table (1) we report the CaSSIS ( $RA_C$ ) and HiRISE ( $RA_H$ ) RSL relative albedos, their  
327 difference and their  $1\sigma$  uncertainties. We obtain average relative albedos of  $\bar{R}A_H =$   
328  $0.792 \pm 0.032$  for HiRISE and  $\bar{R}A_C = 0.790 \pm 0.029$  for CaSSIS. These are broadly  
329 consistent with the relative albedo values measured by Schaefer et al. (2019) between



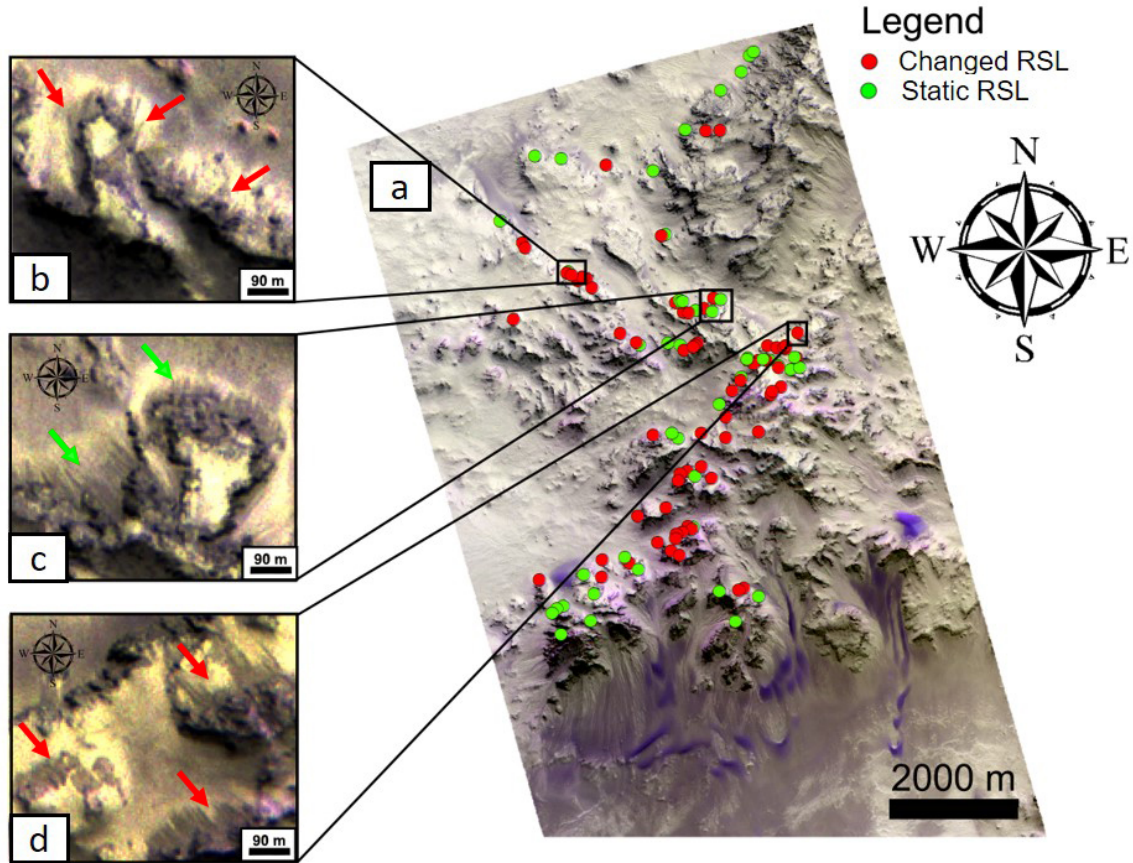


Figure 7: a) RGB color composite of the RED, PAN and BLU filters of CaSSIS image MY34.005640.218.2 depicting the central peak of Hale crater. Red dots indicate “changed” RSL. Green dots indicate “static” RSL. b), c) and d): examples of identified RSL, indicated by black arrows.

330  $L_s = 330^\circ$  and  $L_s = 343^\circ$  at Tivat crater, prior to the fading of RSL, confirming that  
 331 any possible seasonal pattern is not influencing our measurements. The RSL relative  
 332 albedo values reported for each ROI in table (1) show that there are no significant  
 333 differences between the HiRISE and CaSSIS observations. The uncertainty on the  
 334 relative albedo differences in table (1) is given by the sum of the uncertainties on



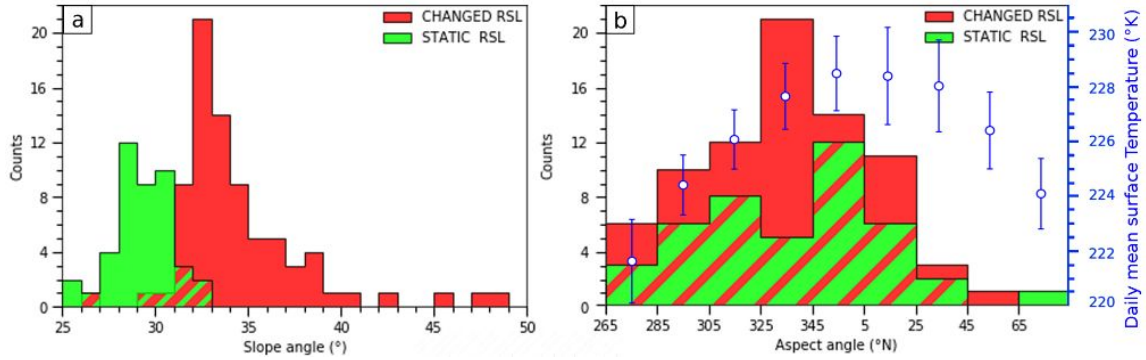


Figure 8: Distributions of a) slope and b) aspect of the termination points for “static” (green) and “changed” (red) RSL. The red-green striped part highlights where the two distributions overlap. The blue dots in b) are daily mean surface temperatures for each aspect bin for the region in figure (5). Error bars indicate the standard deviation within each aspect bin.

335  $RA_C$  and  $RA_H$  and gives us an idea of the minimum albedo difference detectable  
 336 by our methodology. We obtain a mean absolute uncertainty on  $RA_C - RA_H$  of  
 337 0.09, corresponding to an average relative uncertainty of 11%. The relative albedo  
 338 differences reported in table (1) are fully consistent with stochastic variability in  
 339 the two datasets. To demonstrate this, we checked whether the differences between  
 340 the HiRISE and CaSSIS relative albedos follow a normal distribution, applying both  
 341 an Anderson-Darling and a Shapiro-Wilk test of normality. We obtained  $p$ -values  
 342 of  $P_{AD} = 0.48$  and  $P_{SW} = 0.50$ . These are greater than the customary  $\alpha = 0.05$   
 343 threshold, so we cannot reject the null hypothesis that the relative albedo differences  
 344 come from a normal distribution, i.e that they are stochastic. To further cross-check  
 345 our results, we also applied a Kolmogorov-Smirnov and a Wilcoxon signed-rank test  
 346 and assessed the hypothesis that the HiRISE and CaSSIS relative albedos are drawn  
 347 from the same distribution. Both tests failed to reject the null hypothesis, resulting  
 348 in  $p$ -values of  $P_{KS} = 0.99$  and  $P_W = 0.90$  both greater than the  $\alpha = 0.05$  threshold,

ROI	$RA_C$	$RA_H$	$RA_C - RA_H$
1	$0.76 \pm 0.03$	$0.79 \pm 0.06$	$-0.03 \pm 0.09$
2	$0.73 \pm 0.03$	$0.76 \pm 0.05$	$-0.03 \pm 0.08$
3	$0.79 \pm 0.02$	$0.77 \pm 0.06$	$0.02 \pm 0.09$
4	$0.80 \pm 0.02$	$0.75 \pm 0.05$	$0.05 \pm 0.07$
5	$0.78 \pm 0.03$	$0.75 \pm 0.05$	$0.03 \pm 0.08$
6	$0.83 \pm 0.04$	$0.80 \pm 0.06$	$0.03 \pm 0.10$
7	$0.82 \pm 0.03$	$0.85 \pm 0.06$	$-0.02 \pm 0.08$
8	$0.76 \pm 0.02$	$0.81 \pm 0.08$	$-0.05 \pm 0.10$
9	$0.83 \pm 0.04$	$0.79 \pm 0.06$	$0.04 \pm 0.10$
10	$0.79 \pm 0.02$	$0.79 \pm 0.06$	$0.00 \pm 0.08$
11	$0.81 \pm 0.03$	$0.82 \pm 0.07$	$-0.01 \pm 0.10$

Table 1: Relative albedo analysis results.  $RA_C$  and  $RA_H$  are the relative albedos of RSL with respect to nearby RSL-free slopes measured on CaSSIS and HiRISE images, respectively.  $RA_C - RA_H$  is the difference between the CaSSIS and HiRISE relative albedo. Errors are reported as  $1\sigma$  uncertainties.

349 confirming that the detected differences between the HiRISE and CaSSIS relative  
350 albedos are stochastic.

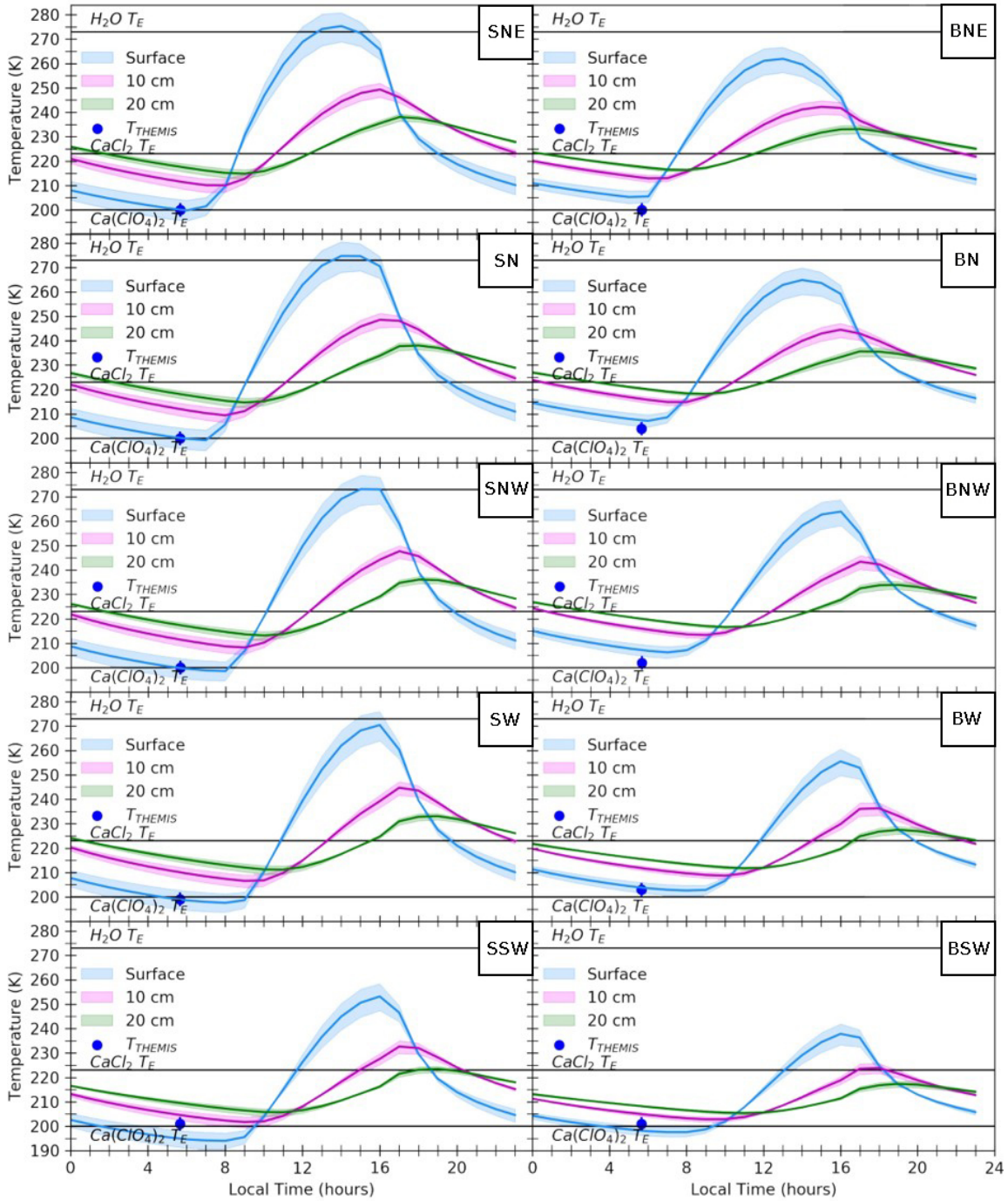


Figure 9: Diurnal temperature profiles (solid lines) with  $3\sigma$  uncertainties (shaded areas) simulated at the surface (light blue), at 10 cm (magenta) and 20 cm depth (green) for the "Slope" (left) and "Bedrock" (right) ROIs defined in figure (5). Blue dots are mean THEMIS surface temperature of each ROI with  $3\sigma$  uncertainties of 2.8 K (Ferguson et al., 2006).

351 *4.3. Thermal analysis*

352 We simulated the thermal environment in a small region within Hale crater,  
353 shown in figure (5). Diurnal surface and subsurface temperature profiles and their  
354 uncertainties for each of the zones in figure (5) are shown in figure (9). In the same  
355 figures, we also show the eutectic temperatures of water ice,  $\text{CaCl}_2$  brine (Gough  
356 et al., 2016) and Ca-perchlorate (Marion et al., 2010), as well as mean THEMIS  
357 surface temperatures for each ROI. From the temperature profiles in figures (9)  
358 we can see that both north-west, north and north-east regions transiently reach  
359 temperatures higher than the melting temperature of water ice only at the regolith  
360 surface, and not on bedrock or in the subsurface. In contrast, the transient melting  
361 of  $\text{CaCl}_2$  or  $\text{Ca}(\text{ClO}_4)_2$  frozen brines is generally supported in all these zones. In  
362 particular, from the temperature profiles in figure (9a) we see that north-east facing  
363 slopes allow the melting of  $\text{CaCl}_2$  at 10 cm in the subsurface from  $\sim 10:00$  local time  
364 until  $\sim$  midnight, and at 20 cm depth from  $\sim 12:00$  to  $\sim 14:00$ . On north facing  
365 slopes (see figure (9b)) melting could occur from  $\sim 11:00$  to  $\sim$  midnight at 10 cm  
366 depth and from  $\sim 13:00$  to  $\sim 15:00$  at 20 cm depth. On north-west facing slopes  
367 (see figure (9c)) melting happens from  $\sim 12:00$  until  $\sim$  midnight at 10 cm depth and  
368 from  $\sim 14:00$  to  $\sim 15:00$  at 20 cm depth. West facing slopes (see figure (9d)) allow  
369 melting of from  $\sim 13:00$  until  $\sim 23:00$  local time at 10 cm depth, and from  $\sim 15:00$   
370 to  $\sim$  midnight at 20 cm depth. Finally, south-west facing slopes permit melting of  
371  $\text{CaCl}_2$  mostly on the regolith and from  $\sim 15:00$  to 20:00 at 10 cm depth. At 20 cm  
372 depth, temperatures are mostly below the eutectic temperature of  $\text{CaCl}_2$  brines (see  
373 figure (9e)). In all these cases, melting of  $\text{Ca}(\text{ClO}_4)_2$  is allowed at any hour of the

374 day at all depths, except for north-west, west and south-west facing slopes where  
 375 early morning surface temperatures are very close to 200 K and can reach values as  
 376 low as 190K, below the eutectic temperature of this brine.

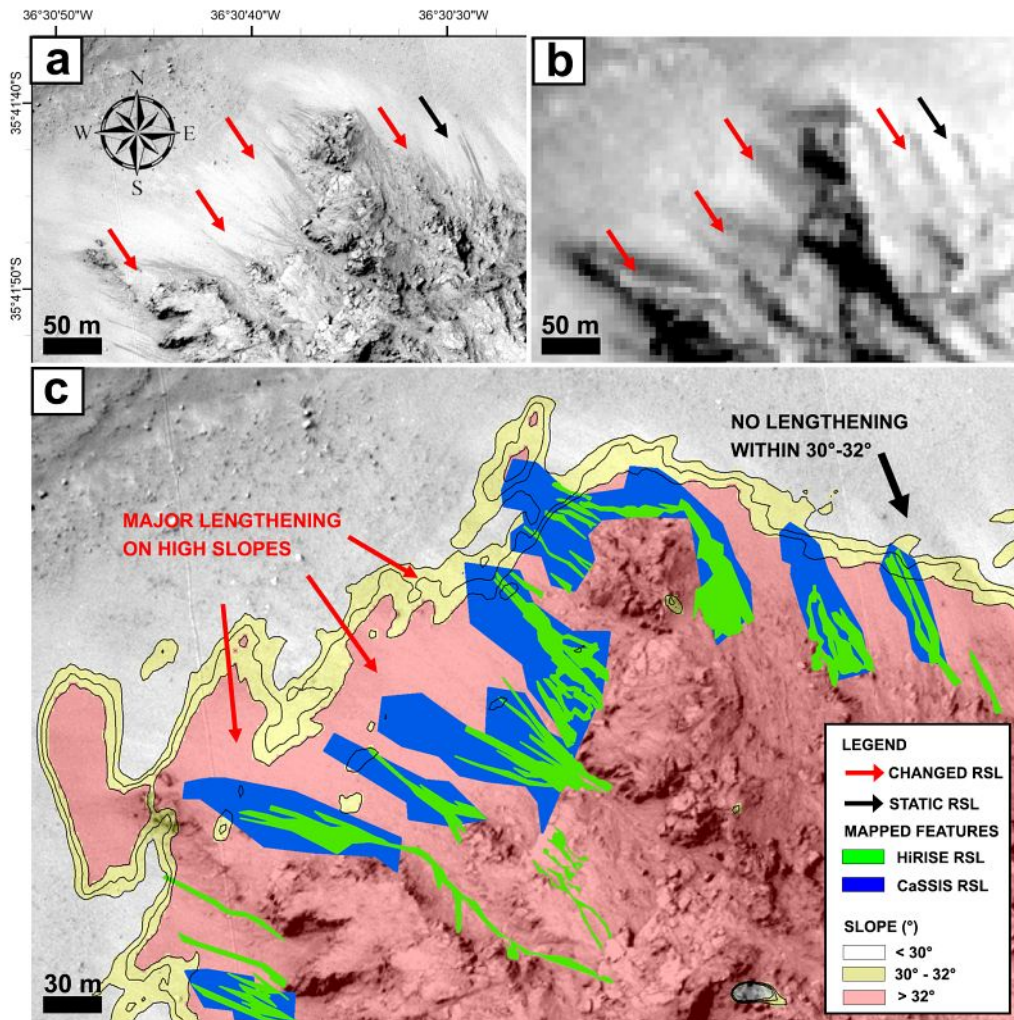


Figure 10: Mapping of HiRISE and CaSSIS RSL. a) HiRISE image depicting both “static” (black arrows) and “changed” RSL (red arrows) on the central peak of Hale crater. b) CaSSIS image showing the same RSL as in panel a). c) Mapping of HiRISE (green) and CaSSIS (blue) RSL overlain on a discretized slope map. The red part is where slopes are  $> 32^\circ$ , the yellow part is for slopes between  $30^\circ$  and  $32^\circ$ .



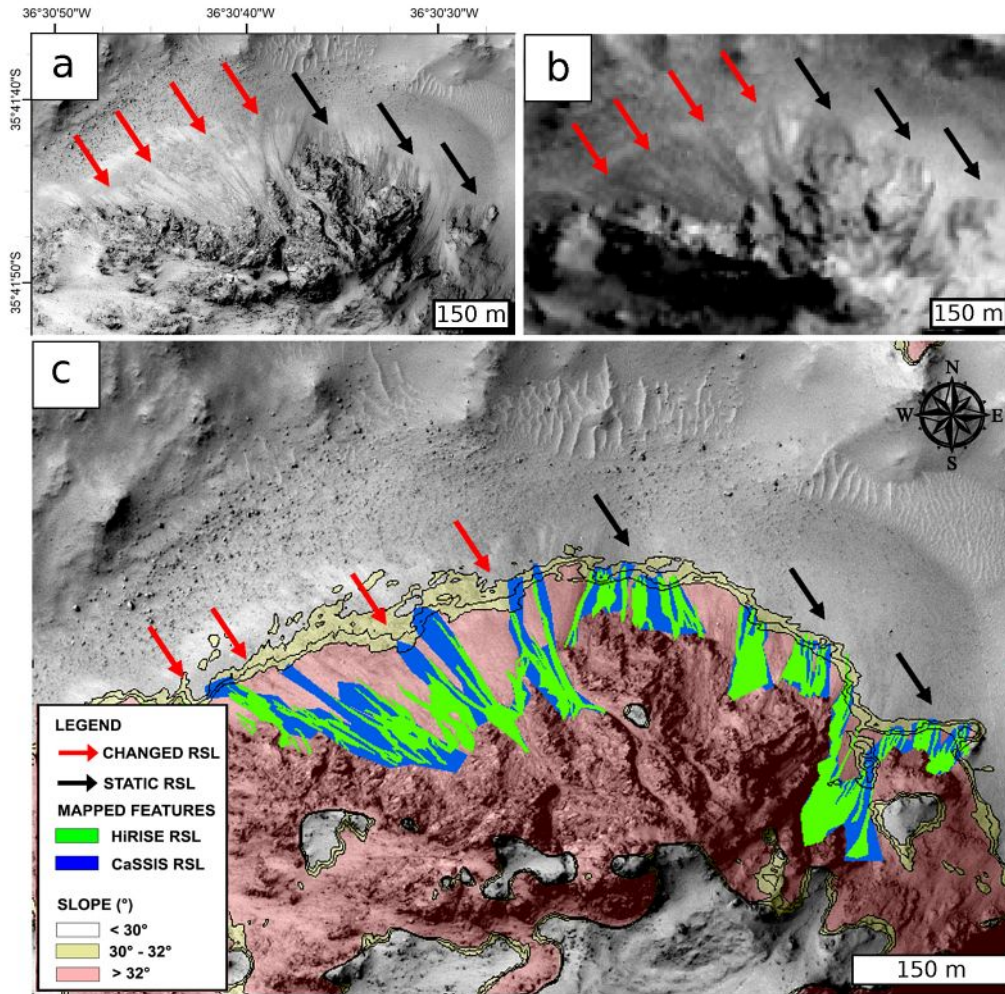


Figure 11: Mapping of HiRISE and CaSSIS RSL. a) HiRISE image depicting both “static” (black arrows) and “changed” RSL (red arrows) on the central peak of Hale crater. b) CaSSIS image showing the same RSL. c) Mapping of HiRISE (green) and CaSSIS (blue) RSL overlain on a discrete slope map. The red part is where slopes are  $> 32^\circ$ , the yellow part is for slopes between  $30^\circ$  and  $32^\circ$ .

## 377 5. Discussion

378 Since at Hale we observe RSL starting on bedrock outcrops (figure (10c)), which  
 379 generally have lower temperatures than the freezing point of water ice but higher

380 than the considered brines, the latter are more likely than flows of seeping water.  
381 Moreover, exposed water ice is not predicted to form on equator-facing slopes at  
382 latitudes comparable to that of Hale crater (Schorghofer et al., 2019), and it is not  
383 observed by spectral instruments sensitive to micrometer-thick surfaces of water frost  
384 (Vincendon et al., 2010). Liquid brines may form via a) melting of a subsurface reser-  
385 voir or b) deliquescence of salts. In the first case, either a reservoir near the surface  
386 or a subsurface deposit, which would be exposed by fractures, are necessary. The  
387 fractured rocky outcrops in the central peak of Hale crater might host these shallow  
388 brine reservoirs. In such a case, brine melting would occur when subsurface tem-  
389 peratures rise above their eutectic temperature, i.e. from mid-afternoon to evening  
390 hours, depending on its depth and slope orientation. This is because ice is more  
391 likely to be found in the shallow subsurface than at the surface at these latitudes.  
392 In particular, our thermal analysis suggests that melting of  $\text{CaCl}_2$  brines should be  
393 favored on north-east, followed by north, north-west, west and south-west facing  
394 slopes. Melting of  $\text{Ca}(\text{ClO}_4)_2$  brine is generally possible on all slopes, as it can oc-  
395 cur over most of a Martian day. However north-east, north and north-west facing  
396 slopes are favored since their subsurface temperature is always higher than 200K at  
397  $L_s = 347.4^\circ$ . This can also be explained by considering the dependence of daily mean  
398 surface temperature from the slope aspect, depicted in figure (8). This predicts that  
399 north-east, north and north-west facing slopes have the highest daily mean surface  
400 temperatures. As a consequence, brines melting is favoured on these slopes. This  
401 picture hence suggests that if RSL are formed through melting of shallow subsurface  
402 brines, they should form and lengthen from noon and early-afternoon to evening

403 hours favouring north-east, north and north-west facing slopes.

404 In the case of deliquescence, the main parameters constraining RSL activity are sur-  
405 face temperature and relative humidity. As shown in figure (9) surface temperatures  
406 are above the eutectic temperature of  $\text{CaCl}_2$  from  $\sim 8:00$  to  $\sim 19:00-20:00$  Mars  
407 local time, depending on the slope orientation and thermal inertia. However, the  
408 RH may not be high enough during these hours. In particular, (Steele et al., 2017)  
409 and (Fischer et al., 2019) show that from  $\sim 8:00$  to  $\sim 19:00-20:00$ , RH values are  
410 below 5% both at Gale crater and at the Phoenix landing site during local summer.  
411 This makes perchlorates more interesting candidates, because surface temperatures  
412 are above their eutectic temperature at any time of day, except for north-west, west  
413 and south-west facing and slopes during early morning. If RSL are deliquescence-  
414 related features, we should see a similar aspect preference as that expected for the  
415 melting of brines, but more shifted towards north-east facing slopes. In fact, these  
416 slopes reach higher surface temperatures at earlier local times, at a time when air  
417 relative humidity is higher (Gough et al., 2016; Steele et al., 2017; Fischer et al.,  
418 2019), which enhances deliquescence. The aspect distribution in figure (8b) suggests  
419 quite a different picture, showing a preference for north, north-west and west facing  
420 slopes over north-east facing slopes. An example of this behavior is also illustrated  
421 in figures (10) and (11) where RSL sourcing from north-east facing slopes are fewer  
422 in number and less extensive than on north, north-west and even west facing slopes.  
423 This aspect distribution may be an indication that RSL lengthening is not associated  
424 with surface moisture, deliquescence of salts or melting of brines. Another option  
425 may instead be that deliquescence occurs during sunset instead of early morning



426 when temperatures fall and relative humidity rises, as suggested by (Tebolt et al.,  
427 2020). In this case, west-facing, north-west and north facing slopes may be favoured  
428 as they have slightly higher evening surface temperatures, possibly explaining the  
429 aspect distribution at Hale crater. While this is in principle consistent with our as-  
430 pect distribution, it is not supported by either laboratory experiments (Gough et al.,  
431 2016), REMS (Steele et al., 2017) or TECP data (Fischer et al., 2019), which suggest,  
432 instead, that early morning hours should be more favourable for deliquescence than  
433 evening hours. Moreover, it may not be in agreement with the very low water con-  
434 tent of RSL estimated from nighttime IR observations (Edwards and Piqueux, 2016).  
435 Detailed, high-resolution modeling may be necessary to further explore the precise  
436 interplay between temperature and relative humidity at RSL locations and quantify  
437 the best periods for deliquescence. An indication that RSL at Hale crater may be  
438 dry flows is that their lengthening stops at slope angles  $\sim 30^\circ$  (Dundas et al., 2017).  
439 We also detect this behavior in our slope distribution in figure (8a) and in figures  
440 (10,11), which show that RSL lengthening is generally correlated with the presence  
441 of slopes steeper than  $\sim 30^\circ - 32^\circ$ . On the contrary, RSL that already reached slopes  
442 within this range or shallower remained static. This dichotomy is shown in figure  
443 (8a), where there is a significant difference between the “changed” and “static” slope  
444 distributions. This dichotomy is expected for dry flows that stop when they reach  
445 the angle of repose, producing the observed sample of “static” RSL, and lengthen  
446 on steeper slopes, producing the observed sample of “changed” RSL. In one case, we  
447 also detect a RSL that lengthened at a slope angle of  $\sim 26^\circ$ . A similar behaviour has  
448 also been detected by Stillman et al. (2020) and Tebolt et al. (2020). Although, in

449 principle, this would support wet-based flows, the fact that they occur with a very  
450 low frequency suggests that these RSL could be statistical outliers (Stillman et al.,  
451 2020). As such, it is possible that additional and/or different mechanisms may be at  
452 play in this sample of RSL. Dedicated analyses considering statistically significant  
453 occurrences of these RSL and consideration of uncertainties in the DTM used for  
454 computing the slope values may be necessary to reach a definitive conclusion. Our  
455 comparison of HiRISE and CaSSIS RSL relative albedo indicates that there are no  
456 significant diurnal variations between 11:13 and 14:06 local time, a result expected  
457 for dry flows. However, it may be also possible that significant dehydration has  
458 already occurred at 11:13, producing the observed result independently from how  
459 RSL form, or that the relative albedo differences at play are lower than 11%. If  
460 RSL are formed through deliquescence, the importance of this issue depends on salt  
461 composition and its interaction with the regolith, as these both affect the DRH and  
462 ERH (efflorescence relative humidity) of the solution (Nuding et al., 2014). In par-  
463 ticular, Nuding et al. (2014) showed that liquid  $\text{Ca}(\text{ClO}_4)_2$  brines persist with very  
464 low RH values. Therefore, if liquid brines form on early morning they may persist  
465 until late morning in a metastable state and dehydrate during the afternoon. Again,  
466 detailed near-surface relative humidity modeling should be performed to determine  
467 whether these processes are occurring at RSL sites. Another interpretation of our  
468 relative albedo measurement, which is not supported by thermal studies (Edwards  
469 and Piqueux, 2016), is that the water supply exceeds evaporative losses. In this case  
470 dehydration does not occur and there is no significant albedo variation (Hillel, 2004).  
471 Future observations acquired during early morning will help to better characterize

472 the diurnal albedo of RSL. Nevertheless, the relative albedo measurements reported  
473 here could provide a useful validation for modeling and experimental studies of RSL.

474 In summary, our result collectively support dry flows as responsible for RSL  
475 lengthening. The triggering mechanisms which initiate these flows may involve ther-  
476 mal creep (Schmidt et al., 2017; Schaefer et al., 2019), or aeolian processes (Vin-  
477 cendon et al., 2019). In particular, the latter would also be able to describe the  
478 temporal evolution of RSL activity during the third pulse shown in figure (1) (Vin-  
479 cendon et al., 2019). While our results support dry flows models, brines and more  
480 generally volatiles may still play an indirect and concurrent role in RSL formation  
481 by triggering dry mass fluxes (Massé et al., 2016; Wang et al., 2019; Bishop et al.,  
482 2019), but our data does not provide any additional insight on RSL triggering.

## 483 **6. Summary and Conclusions**

484 We presented the first CaSSIS observation of RSL obtained during local morning  
485 at Hale crater, Mars. We identified a set of 125 RSL and studied their overall  
486 morphology, slope and aspect distributions and analyzed their thermal environment.  
487 We performed an initial comparison of their relative albedo using morning CaSSIS  
488 and afternoon HiRISE observations. Our comparison of RSL, as viewed through  
489 HiRISE and CaSSIS, 30 days later, reveals that most RSL lengthening occurred  
490 where slopes  $> 30^\circ - 32^\circ$  were available. Instead, RSL on slopes  $> 30^\circ - 32^\circ$  remained  
491 generally static. This result supports a dry granular flow dynamics, as suggested by  
492 other authors (Dundas et al., 2017; Vincendon et al., 2019; Schaefer et al., 2019;  
493 McEwen et al., 2019). The simulated diurnal surface and subsurface temperature

494 profiles at Hale crater suggest that melting of brines and deliquescence of salts would  
495 be both favoured on north-east facing slopes, followed by north and north-west facing  
496 slopes. However, this pattern is different from our observed aspect distribution of  
497 “changed” RSL at Hale crater, suggesting that RSL lengthening is not controlled by  
498 surface moisture, deliquescence of salts or melting of brines. We compared HiRISE  
499 and CaSSIS RSL relative albedo between 11:13 and 14:06 local time, respectively,  
500 and found no significant differences, another result expected for dry flows. Our  
501 measurements could provide a useful validation for future models and experimental  
502 studies on RSL formation and lengthening. We conclude that the RSL at Hale  
503 crater are best explained as dry flows, in agreement with the conclusions of other  
504 authors (Dundas et al., 2017; Vincendon et al., 2019; Schaefer et al., 2019; McEwen  
505 et al., 2019). These may be triggered through thermal creep (Schmidt et al., 2017;  
506 Schaefer et al., 2019), aeolian processes (Vincendon et al., 2019), or very limited brine  
507 activity (Massé et al., 2016; Wang et al., 2019; Bishop et al., 2019). Future CaSSIS  
508 observations of RSL sites acquired earlier in the morning, in combination with same-  
509 day afternoon HiRISE images, will be pivotal in improving the characterization of  
510 the diurnal activity of RSL and will provide a clearer picture of their formation  
511 mechanism.

## 512 **7. Acknowledgments**

513 We would like to thank Dr. Mathieu Vincendon and Dr. Mauro Spagnuolo for  
514 their important and constructive comments that led to a great improvement of the  
515 manuscript. The authors also wish to thank the spacecraft and instrument engineer-

516 ing teams for the successful completion of the instrument. CaSSIS is a project of the  
517 University of Bern and funded through the Swiss Space Office via ESA's PRODEX  
518 programme. The instrument hardware development was also supported by the Ital-  
519 ian Space Agency (ASI) (ASI-INAF agreement no.I/018/12/0), INAF/Astronomical  
520 Observatory of Padova, and the Space Research Center (CBK) in Warsaw. Support  
521 from SGF (Budapest), the University of Arizona (Lunar and Planetary Lab.) and  
522 NASA are also gratefully acknowledged. The relative albedo measurement presented  
523 in table (1) can be found online at <http://doi.org/10.5281/zenodo.3591990>. The  
524 study has been supported by the Italian Space Agency (ASI-INAF agreement no.  
525 2017-03-17). SJC acknowledges the French Space Agency CNES for supporting her  
526 HiRISE and CaSSIS related work.

#### 527 **Declaration of competing interest**

528 The authors declare that they have no known competing financial interests or  
529 personal relationships that could have appeared to influence the work reported in  
530 this paper

531 **Appendix**

532 In Appendix A we report some details of the products used for the analysis,  
 533 such as image IDs, resolution, solar longitude, local solar time, incidence, emission  
 534 and phase angles. In Appendix B we show details on the error propagation for  
 535 computation of relative albedo uncertainties.

536 **Appendix A. Dataset details**

537 We report in table (A.2) some details on the data products defined in section (2)  
 of the main text.

Product type	ID	Resolution m	$L_s$ ( $^\circ$ )	LTST hh:mm	Incidence ( $^\circ$ )	Emission ( $^\circ$ )	Phase ( $^\circ$ )
HiRISE orthoimage	ESP_031203_1440_RED_C_01_ORTHO	0.25	287.7	14:40	37.0 <sup>†</sup>	13.9 <sup>†</sup>	23.5 <sup>†</sup>
HiRISE Image	ESP_058618_1445_RED	0.50	331.5	14:06	37.0	4.0	40.7
HiRISE DTM	DTEEC_030715_1440_030570_1440_A01	1.00					
CaSSIS stereo image 1	MY34_005640_218_1	4.65	347.4	11:13	32.8	11.4	23.4
CaSSIS stereo image 2	MY34_005640_218_2	4.65	347.4	11:13	32.8	10.6	40.1
THEMIS IR image	I01144003	100.00	344.1	03 : 18	119.1	0.7	118.7
THEMIS IR image	I59655010	100.00	348.4	05 : 40	84.6	1.9	84.4
THEMIS IR image	I67826009	100.00	341.1	06 : 30	91.2	0.7	91.1

Table A.2: Summary of the products used in the analysis. Solar longitude ( $L_s$ ), Local time (LTST), incidence, emission and phase angles are taken from <https://www.uahirise.org> for HiRISE, and from <http://viewer.mars.asu.edu/> for THEMIS. <sup>†</sup>The reported incidence, emission and phase angle refers to the corresponding HiRISE Reduced Data Record (RDR) product.

538

539 **Appendix B. Relative albedo uncertainty**

540 We defined the relative albedo (see text for details) as:

$$RA_* = \frac{IF_{RSL} - IF_D}{IF_{BK} - IF_D} \quad * = H, C \quad (\text{B.1})$$

541 where  $RA_*$  is the RSL relative albedo and  $*$  is  $H$  for HiRISE and  $C$  for CaSSIS.  
 542  $IF_{RSL}$  is the mean I/F extracted from an RSL ROI.  $IF_D$  is the I/F of the darkest  
 543 shadowed pixel and  $IF_{BK}$  is the I/F of a BK ROI. To compute the uncertainties in  
 544 our relative albedo measurements, we used a standard error propagation approach.  
 545 In particular, we performed the following approximation:

$$\sigma_{IF_{RSL}-IF_D} \sim 2 \cdot \sigma_{IF_{RSL}} \quad (\text{B.2})$$

$$\sigma_{IF_{BK}-IF_D} \sim 2 \cdot \sigma_{IF_{BK}} \quad (\text{B.3})$$

546 where  $\sigma_{IF_{RSL}-IF_D}$  and  $\sigma_{IF_{BK}-IF_D}$  are the uncertainties of the numerator and denom-  
 547 inator of equation (B.1). This approximation is justified for two reasons: first, we  
 548 do not have an unambiguous way to define a ROI within shadows in and retrieve  
 549 its mean flux and its standard deviation. Second, we do not know the errors on the  
 550 HiRISE or CaSSIS radiometric calibration equations and thus we cannot propagate  
 551 the uncertainty on the Digital Number (DN) of the darkest shadowed pixel. Instead,  
 552 we can reasonably expect its uncertainty to be of the same order of magnitude as  
 553 the uncertainty in  $IF_{RSL}$  and  $IF_{BK}$ . With this approximation, the uncertainty on  
 554 relative albedo measurements may be propagated as:

$$\begin{aligned}\sigma_{A_*} &= \sqrt{\left(\frac{\partial A_*}{\partial(IF_{RSL} - IF_D)}\sigma_{IF_{RSL}-IF_D}\right)^2 + \left(\frac{\partial A_*}{\partial(IF_{BK} - IF_D)}\sigma_{IF_{BK}-IF_D}\right)^2} = \\ &= A_*\sqrt{\left(\frac{2\sigma_{IF_{RSL}}}{IF_{RSL} - IF_D}\right)^2 + \left(\frac{2\sigma_{IF_{BK}}}{IF_{BK} - IF_D}\right)^2}\end{aligned}$$

555 **References**

556 A. Z. Abotalib and E. Heggy. A deep groundwater origin for recurring slope lineae on  
557 Mars. *Nature Geoscience*, 12:235–241, Mar. 2019. doi: 10.1038/s41561-019-0327-5.

558 T. W. Anderson and D. A. Darling. A test of goodness of fit. *Journal of the*  
559 *American Statistical Association*, 49(268):765–769, 1954. doi: 10.1080/01621459.  
560 1954.10501232.

561 J. L. Bishop, J. D. Toner, P. Englert, V. C. Gulick, A. S. McEwen, Z. F. M. Burton,  
562 M. F. Thomas, E. K. Gibson, and C. Koeberl. Salty Solution to Slipping Soils on  
563 Martian Slopes. In *Lunar and Planetary Science Conference*, Lunar and Planetary  
564 Science Conference, page 1188, Mar 2019.

565 P. A. Burrough and R. A. McDonell. *Principles of Geographical Information Systems*  
566 . Oxford University Press, New York, 1998.

567 V. F. Chevrier and E. G. Rivera-Valentin. Formation of recurring slope lineae by  
568 liquid brines on present-day mars. *Geophysical Research Letters*, 39(21), 2012.



569 doi: 10.1029/2012GL054119. URL <https://agupubs.onlinelibrary.wiley.com/doi/abs/10.1029/2012GL054119>.  
570

571 M. Chojnacki, A. McEwen, C. Dundas, L. Ojha, A. Urso, and S. Sutton. Geo-  
572 logic context of recurring slope lineae in melas and coprates chasmata, mars.  
573 *Journal of Geophysical Research: Planets*, 121(7):1204–1231, 2016. doi: 10.  
574 1002/2015JE004991. URL <https://agupubs.onlinelibrary.wiley.com/doi/abs/10.1002/2015JE004991>.  
575

576 P. R. Christensen, B. M. Jakosky, H. H. Kieffer, M. C. Malin, J. McSween,  
577 Harry Y., K. Nealson, G. L. Mehall, S. H. Silverman, S. Ferry, M. Caplinger,  
578 and M. Ravine. The Thermal Emission Imaging System (THEMIS) for the  
579 Mars 2001 Odyssey Mission. *Space Sci. Rev.*, 110(1):85–130, Jan 2004. doi:  
580 10.1023/B:SPAC.0000021008.16305.94.

581 I. J. Daubar, C. M. Dundas, S. Byrne, P. Geissler, G. D. Bart, A. S. McEwen,  
582 P. S. Russell, M. Chojnacki, and M. P. Golombek. Changes in blast zone albedo  
583 patterns around new martian impact craters. *Icarus*, 267:86–105, Mar 2016. doi:  
584 10.1016/j.icarus.2015.11.032.

585 C. M. Dundas, A. S. McEwen, M. Chojnacki, M. P. Milazzo, S. Byrne, J. N. McEl-  
586 waine, and A. Urso. Granular flows at recurring slope lineae on Mars indicate a  
587 limited role for liquid water. *Nature Geoscience*, 10(12):903–907, Dec 2017. doi:  
588 10.1038/s41561-017-0012-5.

589 C. S. Edwards and S. Piqueux. The water content of recurring slope lineae on

590 Mars. *Geophysical Research Letters*, 43(17):8912–8919, Sep 2016. doi: 10.1002/  
591 2016GL070179.

592 R. L. Fergason, P. R. Christensen, and H. H. Kieffer. High-resolution thermal inertia  
593 derived from the Thermal Emission Imaging System (THEMIS): Thermal model  
594 and applications. *Journal of Geophysical Research (Planets)*, 111(E12):E12004,  
595 Dec 2006. doi: 10.1029/2006JE002735.

596 E. Fischer, G. M. Martínez, N. O. Rennó, L. K. Tamppari, and A. P. Zent.  
597 Relative humidity on mars: New results from the phoenix tecp sensor. *Jour-  
598 nal of Geophysical Research: Planets*, 124(11):2780–2792, 2019. doi: 10.1029/  
599 2019JE006080. URL [https://agupubs.onlinelibrary.wiley.com/doi/abs/  
600 10.1029/2019JE006080](https://agupubs.onlinelibrary.wiley.com/doi/abs/10.1029/2019JE006080).

601 R. V. Gough, V. F. Chevrier, and M. A. Tolbert. Formation of liquid water at low  
602 temperatures via the deliquescence of calcium chloride: Implications for Antarctica  
603 and Mars. *Planet. Space Sci.*, 131:79–87, Oct 2016. doi: 10.1016/j.pss.2016.07.006.

604 R. E. Grimm, K. P. Harrison, and D. E. Stillman. Water budgets of martian  
605 recurring slope lineae. *Icarus*, 233:316 – 327, 2014. ISSN 0019-1035. doi:  
606 <https://doi.org/10.1016/j.icarus.2013.11.013>. URL [http://www.sciencedirect.  
607 com/science/article/pii/S0019103513004764](http://www.sciencedirect.com/science/article/pii/S0019103513004764).

608 J. Gross and U. Ligges. *nortest: Tests for Normality*, 2015. URL [https://CRAN.  
609 R-project.org/package=nortest](https://CRAN.R-project.org/package=nortest). R package version 1.0-4.

610 D. Hillel. *Introduction to environmental soil physics*. Elsevier Science & Technology,  
611 2004.

612 N. Hoekzema, M. Garcia-Comas, O. Stenzel, E. Petrova, N. Thomas, W. Markiewicz,  
613 K. Gwinner, H. Keller, and W. Delamere. Retrieving optical depth from shadows  
614 in orbiter images of mars. *Icarus*, 214(2):447 – 461, 2011. ISSN 0019-1035. doi:  
615 <https://doi.org/10.1016/j.icarus.2011.06.009>. URL <http://www.sciencedirect.com/science/article/pii/S0019103511002181>.

617 C. Huber, L. Ojha, L. Lark, and J. W. Head. Physical models and predictions for  
618 Recurring Slope Lineae formed by wet and dry processes. *Icarus*, 335:113385, Jan  
619 2020. doi: 10.1016/j.icarus.2019.07.019.

620 E. K. Leask, B. L. Ehlmann, M. M. Dundar, S. L. Murchie, and F. P. Seelos. Chal-  
621 lenges in the Search for Perchlorate and Other Hydrated Minerals With 2.1- $\mu\text{m}$   
622 Absorptions on Mars. *Geophys. Res. Lett.*, 45(22):12,180–12,189, Nov 2018. doi:  
623 10.1029/2018GL080077.

624 J. Levy. Hydrological characteristics of recurrent slope lineae on mars: Evidence for  
625 liquid flow through regolith and comparisons with antarctic terrestrial analogs.  
626 *Icarus*, 219(1):1 – 4, 2012. ISSN 0019-1035. doi: [https://doi.org/10.1016/j.](https://doi.org/10.1016/j.icarus.2012.02.016)  
627 [icarus.2012.02.016](https://doi.org/10.1016/j.icarus.2012.02.016). URL [http://www.sciencedirect.com/science/article/](http://www.sciencedirect.com/science/article/pii/S0019103512000644)  
628 [pii/S0019103512000644](http://www.sciencedirect.com/science/article/pii/S0019103512000644).

629 J. Levy, A. Nolin, A. Fountain, and J. Head. Hyperspectral measurements of  
630 wet, dry and saline soils from the McMurdo Dry Valleys: soil moisture prop-

631 erties from remote sensing. *Antarctic Science*, 26(5):565–572, Oct 2014. doi:  
632 10.1017/S0954102013000977.

633 G. Marion, D. Catling, K. Zahnle, and M. Claire. Modeling aqueous perchlo-  
634 rate chemistries with applications to mars. *Icarus*, 207(2):675 – 685, 2010.  
635 ISSN 0019-1035. doi: <https://doi.org/10.1016/j.icarus.2009.12.003>. URL <http://www.sciencedirect.com/science/article/pii/S0019103509004904>.

637 M. Massé, S. J. Conway, J. Gargani, M. R. Patel, K. Pasquon, A. McEwen, S. Carpy,  
638 V. Chevrier, M. R. Balme, L. Ojha, M. Vincendon, F. Poulet, F. Costard, and  
639 G. Jouannic. Transport processes induced by metastable boiling water under  
640 Martian surface conditions. *Nature Geoscience*, 9(6):425–428, Jun 2016. doi:  
641 10.1038/ngeo2706.

642 F. J. Massey. The kolmogorov-smirnov test for goodness of fit. *Journal of the*  
643 *American Statistical Association*, 46(253):68–78, 1951. ISSN 01621459. URL <http://www.jstor.org/stable/2280095>.

645 A. S. McEwen, E. M. Eliason, J. W. Bergstrom, N. T. Bridges, C. J. Hansen, W. A.  
646 Delamere, J. A. Grant, V. C. Gulick, K. E. Herkenhoff, L. Keszthelyi, R. o. L.  
647 Kirk, M. T. Mellon, S. W. Squyres, N. Thomas, and C. M. Weitz. Mars Re-  
648 connaissance Orbiter’s High Resolution Imaging Science Experiment (HiRISE).  
649 *Journal of Geophysical Research (Planets)*, 112(E5):E05S02, May 2007. doi:  
650 10.1029/2005JE002605.

651 A. S. McEwen, L. Ojha, C. M. Dundas, S. S. Mattson, S. Byrne, J. J. Wray, S. C.  
652 Cull, S. L. Murchie, N. Thomas, and V. C. Gulick. Seasonal flows on warm martian

653 slopes. *Science*, 333(6043):740–743, 2011. ISSN 0036-8075. doi: 10.1126/science.  
654 1204816. URL <https://science.sciencemag.org/content/333/6043/740>.

655 A. S. McEwen, C. M. Dundas, S. S. Mattson, A. D. Toigo, L. Ojha, J. J. Wray,  
656 M. Chojnacki, S. Byrne, S. L. Murchie, and N. Thomas. Recurring slope lineae  
657 in equatorial regions of Mars. *Nature Geoscience*, 7(1):53–58, Jan 2014. doi:  
658 10.1038/ngeo2014.

659 A. S. McEwen, E. Schafer, S. Sutton, and M. Chojnacki. Abundant Recurring Slope  
660 Lineae (RSL) Following the 2018 Planet-Encircling Dust Event (PEDE). In *Lunar  
661 and Planetary Science Conference*, Lunar and Planetary Science Conference, page  
662 1376, Mar 2019.

663 Z. M. Moratto, M. J. Broxton, R. A. Beyer, M. Lundy, and K. Husmann. Ames Stereo  
664 Pipeline, NASA’s Open Source Automated Stereogrammetry Software. In *Lunar  
665 and Planetary Science Conference*, volume 41 of *Lunar and Planetary Science  
666 Conference*, page 2364, Mar. 2010.

667 D. Nuding, E. Rivera-Valentin, R. Davis, R. Gough, V. Chevrier, and M. Tol-  
668 bert. Deliquescence and efflorescence of calcium perchlorate: An investiga-  
669 tion of stable aqueous solutions relevant to mars. *Icarus*, 243:420 – 428, 2014.  
670 ISSN 0019-1035. doi: <https://doi.org/10.1016/j.icarus.2014.08.036>. URL [http:  
671 //www.sciencedirect.com/science/article/pii/S0019103514004527](http://www.sciencedirect.com/science/article/pii/S0019103514004527).

672 L. Ojha, A. McEwen, C. Dundas, S. Byrne, S. Mattson, J. Wray, M. Masse, and  
673 E. Schaefer. Hirise observations of recurring slope lineae (rsl) during southern

674 summer on mars. *Icarus*, 231:365 – 376, 2014. ISSN 0019-1035. doi: <https://doi.org/10.1016/j.icarus.2013.12.021>. URL <http://www.sciencedirect.com/science/article/pii/S0019103513005393>.  
675  
676

677 L. Ojha, M. B. Wilhelm, S. L. Murchie, A. S. McEwen, J. J. Wray, J. Hanley,  
678 M. Massé, and M. Chojnacki. Spectral evidence for hydrated salts in recurring  
679 slope lineae on Mars. *Nature Geoscience*, 8(11):829–832, Nov 2015. doi: 10.1038/  
680 ngeo2546.

681 A. Pommerol, N. Thomas, B. Jost, P. Beck, C. Okubo, and A. S. McEwen. Photo-  
682 metric properties of mars soils analogs. *Journal of Geophysical Research: Plan-*  
683 *ets*, 118(10):2045–2072, 2013. doi: 10.1002/jgre.20158. URL [https://agupubs.](https://agupubs.onlinelibrary.wiley.com/doi/abs/10.1002/jgre.20158)  
684 [onlinelibrary.wiley.com/doi/abs/10.1002/jgre.20158](https://agupubs.onlinelibrary.wiley.com/doi/abs/10.1002/jgre.20158).

685 N. E. Putzig, E. M. Barratt, M. T. Mellon, and T. I. Michaels. MARSTHERM: A  
686 Web-based System Providing Thermophysical Analysis Tools for Mars Research.  
687 In *AGU Fall Meeting Abstracts*, volume 2013, pages P43C–2023, Dec 2013.

688 R Core Team. *R: A Language and Environment for Statistical Computing*. R  
689 Foundation for Statistical Computing, Vienna, Austria, 2019. URL <https://www.R-project.org/>.  
690

691 E. I. Schaefer, A. S. McEwen, and S. S. Sutton. A case study of recurring slope  
692 lineae (RSL) at Tivat crater: Implications for RSL origins. *Icarus*, 317:621–648,  
693 Jan 2019. doi: 10.1016/j.icarus.2018.07.014.

694 F. Schmidt, F. Andrieu, F. Costard, M. Kocifaj, and A. G. Meresescu. Formation

695 of recurring slope lineae on Mars by rarefied gas-triggered granular flows. *Nature*  
696 *Geoscience*, 10(4):270–273, Mar 2017. doi: 10.1038/ngeo2917.

697 N. Schorghofer, J. Levy, and T. Goudge. High-resolution thermal environ-  
698 ment of recurring slope lineae in palikir crater, mars, and its implications for  
699 volatiles. *Journal of Geophysical Research: Planets*, 0(ja), 2019. doi: 10.1029/  
700 2019JE006083. URL [https://agupubs.onlinelibrary.wiley.com/doi/abs/  
701 10.1029/2019JE006083](https://agupubs.onlinelibrary.wiley.com/doi/abs/10.1029/2019JE006083).

702 S. S. Shapiro and M. B. Wilk. An analysis of variance test for normality (complete  
703 samples). *Biometrika*, 52(3/4):591–611, 1965. ISSN 00063444. URL [http://www.  
704 jstor.org/stable/2333709](http://www.jstor.org/stable/2333709).

705 D. Shoji, S. Imamura, M. Nakamura, and R. Noguchi. Angle of repose of Martian wet  
706 sand using discrete element method: Implication for the seasonal cycle of recurring  
707 slope lineae(RSL) by relative humidity. *arXiv e-prints*, art. arXiv:1909.06144, Sep  
708 2019.

709 E. Simioni, C. Re, T. Mudric, A. Pommerol, N. Thomas, and G. Cremonese. a  
710 Photogrammetric Pipeline for the 3d Reconstruction of Cassis Images on Board  
711 Exomars Tgo. *ISPRS - International Archives of the Photogrammetry, Remote*  
712 *Sensing and Spatial Information Sciences*, 62W1:133–139, Jul 2017. doi: 10.5194/  
713 isprs-archives-XLII-3-W1-133-2017.

714 L. J. Steele, M. R. Balme, S. R. Lewis, and A. Spiga. The water cycle and re-  
715 golith–atmosphere interaction at gale crater, mars. *Icarus*, 289:56 – 79, 2017.

716 ISSN 0019-1035. doi: <https://doi.org/10.1016/j.icarus.2017.02.010>. URL <http://www.sciencedirect.com/science/article/pii/S0019103516304845>.  
717

718 D. E. Stillman and R. E. Grimm. Two pulses of seasonal activity in martian southern  
719 mid-latitude recurring slope lineae (RSL). *Icarus*, 302:126–133, Mar 2018. doi:  
720 10.1016/j.icarus.2017.10.026.

721 D. E. Stillman, T. I. Michaels, R. E. Grimm, and K. P. Harrison. New observations  
722 of martian southern mid-latitude recurring slope lineae (RSL) imply formation by  
723 freshwater subsurface flows. *Icarus*, 233:328–341, May 2014. doi: 10.1016/j.icarus.  
724 2014.01.017.

725 D. E. Stillman, T. I. Michaels, R. E. Grimm, and J. Hanley. Observations and  
726 modeling of northern mid-latitude recurring slope lineae (RSL) suggest recharge  
727 by a present-day martian briny aquifer. *Icarus*, 265:125–138, Feb 2016. doi: 10.  
728 1016/j.icarus.2015.10.007.

729 D. E. Stillman, B. D. Bue, K. L. Wagstaff, K. M. Primm, T. I. Michaels, and  
730 R. E. Grimm. Evaluation of wet and dry recurring slope lineae (rsl) formation  
731 mechanisms based on quantitative mapping of rsl in garni crater, valles marineris,  
732 mars. *Icarus*, 335:113420, 2020. ISSN 0019-1035. doi: <https://doi.org/10.1016/j.icarus.2019.113420>. URL <http://www.sciencedirect.com/science/article/pii/S0019103519303835>.  
734

735 M. Tebolt, J. Levy, T. Goudge, and N. Schorghofer. Slope, elevation, and thermal  
736 inertia trends of martian recurring slope lineae initiation and termination points:



737 Multiple possible processes occurring on coarse, sandy slopes. *Icarus*, 338:113536,  
738 2020. ISSN 0019-1035. doi: <https://doi.org/10.1016/j.icarus.2019.113536>. URL  
739 <http://www.sciencedirect.com/science/article/pii/S0019103519305779>.

740 N. Thomas, G. Cremonese, R. Ziethe, M. Gerber, M. Brändli, G. Bruno, M. Eris-  
741 mann, L. Gambicorti, T. Gerber, K. Ghose, M. Gruber, P. Gubler, H. Mis-  
742 chler, J. Jost, D. Piazza, A. Pommerol, M. Rieder, V. Roloff, A. Servonet,  
743 W. Trottmann, T. Uthaicharoenpong, C. Zimmermann, D. Vernani, M. Johnson,  
744 E. Pelò, T. Weigel, J. Viertl, N. De Roux, P. Lochmatter, G. Sutter, A. Ca-  
745 sciello, T. Hausner, I. Fikai Veltroni, V. Da Deppo, P. Orleanski, W. Nowosielski,  
746 T. Zawistowski, S. Szalai, B. Sodor, S. Tulyakov, G. Troznai, M. Banaskiewicz,  
747 J. C. Bridges, S. Byrne, S. Debei, M. R. El-Maarry, E. Hauber, C. J. Hansen,  
748 A. Ivanov, L. Keszthelyi, R. Kirk, R. Kuzmin, N. Mangold, L. Marinangeli, W. J.  
749 Markiewicz, M. Massironi, A. S. McEwen, C. Okubo, L. L. Tornabene, P. Wajer,  
750 and J. J. Wray. The Colour and Stereo Surface Imaging System (CaSSIS) for the  
751 ExoMars Trace Gas Orbiter. *Space Sci. Rev.*, 212(3-4):1897–1944, Nov 2017. doi:  
752 10.1007/s11214-017-0421-1.

753 J. Toner and D. Catling. Chlorate brines on mars: Implications for the occurrence  
754 of liquid water and deliquescence. *Earth and Planetary Science Letters*, 497:161 –  
755 168, 2018. ISSN 0012-821X. doi: <https://doi.org/10.1016/j.epsl.2018.06.011>. URL  
756 <http://www.sciencedirect.com/science/article/pii/S0012821X18303509>.

757 M. Vincendon, Y. Langevin, F. Poulet, J.-P. Bibring, and B. Gondet. Recovery of  
758 surface reflectance spectra and evaluation of the optical depth of aerosols in the

759 near-ir using a monte carlo approach: Application to the omega observations of  
760 high-latitude regions of mars. *Journal of Geophysical Research: Planets*, 112(E8),  
761 2007. doi: 10.1029/2006JE002845. URL <https://agupubs.onlinelibrary.wiley.com/doi/abs/10.1029/2006JE002845>.

763 M. Vincendon, F. Forget, and J. Mustard. Water ice at low to midlatitudes on  
764 mars. *Journal of Geophysical Research: Planets*, 115(E10), 2010. doi: 10.  
765 1029/2010JE003584. URL <https://agupubs.onlinelibrary.wiley.com/doi/abs/10.1029/2010JE003584>.

767 M. Vincendon, C. Pilorget, J. Carter, and A. Stcherbinine. Observational evidence  
768 for a dry dust-wind origin of mars seasonal dark flows. *Icarus*, 325:115 – 127,  
769 2019. ISSN 0019-1035. doi: <https://doi.org/10.1016/j.icarus.2019.02.024>. URL  
770 <http://www.sciencedirect.com/science/article/pii/S0019103518305712>.

771 A. Wang, Z. Ling, Y. Yan, A. S. McEwen, M. T. Mellon, M. D. Smith, B. L. Jolliff,  
772 and J. Head. Subsurface Cl-bearing salts as potential contributors to recurring  
773 slope lineae (RSL) on Mars. *Icarus*, 333:464–480, Nov 2019. doi: 10.1016/j.icarus.  
774 2019.06.024.

775 F. Wilcoxon. Individual comparisons by ranking methods. *Biometrics Bulletin*, 1  
776 (6):80–83, 1945. ISSN 00994987. URL <http://www.jstor.org/stable/3001968>.